LEBANESE AMERICAN UNIVERSITY

Numerical Investigation of the Use of Flexible Blade for Vertical Axis Wind Turbine

By

Ahmad Hijazi

A thesis

submitted in partial fulfillment of the requirements

for the degree of Master of Science in Mechanical Engineering

School of Engineering

July 2023

THESIS APPROVAL FORM

Student Name: Ahmad Hijazi   I.D. #: 201705807

Thesis Title: Numerical Investigation of the Use of Flexible Blade for Vertical Axis Wind Turbine

Program: Master of Science in Mechanical Engineering

Department: Department of Industrial and Mechanical Engineering

School: School of Engineering

The undersigned certify that they have examined the final electronic copy of this thesis and approved it in Partial Fulfillment of the requirements for the degree of:

Master of Science   in the major of   Mechanical Engineering

Thesis Advisor's Name: Michel ElKhoury

Signature: *M. K.*

Digitally signed by Michel Khoury
DN: cn=Michel Khoury, o=LAU, ou,
email=mkhoury@lau.edu.lb, c=LB
Date: 2023.07.10 16:22:19 +03'00'

Date: 10 / 7 / 2023
      Day   Month   Year

Committee Member's Name: Amne El Cheikh

Signature: Amne

Digitally signed by Amne
DN: cn=Amne, o=Lebanese American University,
ou=LAU, email=amne.elcheikh@lau.edu.lb, c=LB
Date: 2023.07.04 12:11:52 +03'00'

Date: 4 / 7 / 23
      Day   Month   Year

Committee Member's Name: Nadim Zakhia

Signature: Nadim

Date: 5 / 7 / 23
      Day   Month   Year

LAU
الجامعة اللبنانية الأميركية
Lebanese American University

THESIS COPYRIGHT RELEASE FORM

Name: Ahmad Hijazi

Signature: Ahmad

Date: 14/6/2023

PLAGIARISM POLICY COMPLIANCE STATEMENT

I certify that:

1. I have read and understood LAU's Plagiarism Policy.
2. I understand that failure to comply with this Policy can lead to academic and disciplinary actions against me.
3. This work is substantially my own, and to the extent that any part of this work is not my own I have indicated that by acknowledging its sources.

Name: Ahmad Hijazi

Signature: Ahmad

Date: 14/6/2023

ACKNOWLEDGMENT

I would like to express my deepest appreciation to everyone who helped and supported me to complete the work on this research project. I am deeply grateful to my thesis supervisor, Dr. Michel Khoury for his support and guidance throughout my master's program. His expertise and patience have been invaluable to me and have played a crucial role in the success of this thesis.

I would also like to thank Dr. Amne El Chiekh for her continuous support and guidance that helped in the completion of this thesis. Her encouragement and advice have been invaluable throughout this project.

I am also grateful to the Lebanese American University for providing me with the opportunity to conduct my research and for all of the computational resources and support they provided.

I would also like to thank the engineering lab staff, especially Mr. Salim Jamal-Eddine who was always ready to solve any technical issue I faced.

Finally, I want to express my gratitude to my friends and family for their love and support throughout this process. I would not have been able to finish this journey without their support and motivation.

Numerical Investigation of the Use of Flexible Blade for Vertical Axis Wind Turbine

Ahmad Hijazi

ABSTRACT

This study proposes a novel vertical axis wind turbine (VAWT) design with flexible blades aiming to improve their energy extraction capability. The blade deformation is achieved using Ansys Fluent dynamic mesh and user-defined functions to control the position of the blades nodes at specific azimuthal angles. An optimization study is carried out using computational fluid dynamics (CFD) simulations and design of experiments (DOE) to get the optimal design parameters of the flexible blade at different tip speed ratios (TSRs). In addition, a comparison between the DOE results of both 2D and 3D CFD simulations is achieved to assess the use of 2D simulations for optimization purposes. Also, a detailed numerical study of the aerodynamic performance of the turbine based on this new design is done to compare the rigid and flexible blade models' power coefficient and flow fields around the blades. Results of 2D and 3D CFD simulations show that the flexible blades are able to improve the power coefficient of the turbine by up to 66% and 32% respectively at low tip speed ratios diminishing gradually with increasing tip speed ratios. It is also noticeable that similar pattern in power coefficient results was obtained from the 2D and 3D simulations of both turbine models. This in turn indicates that 2D simulations can be used to get a firsthand guess on the trend and location of the optimized design however, will fail to predict the exact improvement.

Keywords : Vertical axis wind turbine, Flexible blade, Dynamic mesh, Design of Experiments, Computational Fluid Dynamics

TABLE OF CONTENTS

LIST OF TABLES

LIST OF FIGURES

Nomenclature

A	Swept Area of wind turbine [m^2]		ω	Angular Velocity [rad/s]
c	Chord length [m]		$V\infty$	Freestream Velocity [m/s]
R	Turbine Radius [m]		ρ	Air Density [Kg/m^3]
β	Blade pitch angle [deg]		$d\theta$	Azimuthal Increment [deg]
H	Height of turbine blade [m]		θ	Azimuth Angle [deg]
D	Turbine Diameter [m]		λ	Tip speed ratio
N	Number of blades		σ	Solidity
Cm	Moment Coefficient		$\dfrac{Cp}{Cpo}$	Turbine Response
Cp	Power Coefficient		T	Torque [N-m]

CHAPTER ONE

INTRODUCTION

During the last few decades, energy demand has increased due to the increase in the world's population and industrial development [1]. Energy sources like fossil fuels are becoming increasingly scarce [2], and environmental challenges such as global warming, unusual weather patterns, and the high emission rates of carbon dioxide are becoming more prevalent [3]. Renewable energy sources, such as wind, solar, and biomass, are alternatives to the conventional energy sources currently being used to overcome these issues and ensure environmental sustainability. Wind energy is a sustainable energy resource that is harvested through wind turbines which convert the kinetic energy of wind into electrical power [4,5].

Wind turbines are divided into two categories depending on the orientation of the rotating axis: Horizontal Axis Wind Turbines (HAWTs) whose axis is parallel to the direction of wind and Vertical Axis Wind Turbines (VAWTs) whose axis is perpendicular to the direction of wind [6,7]. HAWTs are still the commercial option for large scale power production, but VAWTs are gaining a lot of interest in urban environment [7–9]. This interest is due to the low installation and manufacturing costs, low noise pollution, no yaw mechanism due to its omni-directional nature and its performance in turbulent conditions where wind flow is unsteady and unstable [7,10,11]. According to Ghasemian et al. [7] and Xu et al. [12], VAWTs are divided into two categories: Savonius and Darrieus wind turbines. Savonius wind turbines depend on the drag force to operate whereas Darrieus wind turbines depend on the lift force resulting in a higher power performance and efficiency compared to Savonius wind turbines.

Different studies have been done to improve the performance of the wind turbines by investigating the impact of different operational parameters like tip speed ratio, Reynolds number and turbulence intensity, in addition to different geometrical parameters like number of blades, solidity, airfoil shape, pitch angle and blade aspect ratio [13]. Another studies have investigated the effect of passive and active flow control techniques on the performance of the turbine where such techniques are used to delay or eliminate the dynamic stall which is a flow separation resulting from large variation of Angle of attack at low tip speed ratios [14]. In addition, passive flow control techniques are simple, have low cost and

no additional energy consumption [15] whereas active flow control methods are more complex, require more weight, maintenance, and cost [16].

This research will introduce a flow control technique that can be used for vertical axis wind turbine to improve its performance at different tip speed ratios by using a flexible blade that can deform at certain azimuthal angles to extract more energy from the wind and improve the efficiency of the turbine.

Outline of the thesis

The outline of this research can be summarized as follows. A detailed literature review is presented in chapter two, and the aim, objectives and scope of this work is presented in chapter three. The methodology of this study is described in details in chapter four including the computational grid used, the numerical setup and the validation and verification studies. After that, design of experiments (DOE) approach is presented in chapter five, and results and discussion are presented in chapter six including the DOE results and CFD numerical results of the 2D and 3D simulations. Finally, a conclusion is presented in chapter seven.

CHAPTER TWO

LITERATURE REVIEW

Extensive research has been done to improve the aerodynamic performance of vertical axis wind turbines. Some of these studies focused on optimizing the airfoil shape. For example, Ferreira et al. [17] optimized the shape of thick airfoils to be used in VAWTs using a genetic optimization algorithm. De Tavernier et al. [18] used genetic algorithm to optimize the airfoil shape for a multimegawatt VAWT. Even though many airfoils have been designed and optimized for wind turbine applications, there is more room for improvement in the performance of the turbine [1]. And that introduced the use of flexible blades or new materials that can help increase the ability of the turbine to capture more energy from the wind [1]. Such idea allows the turbine blade to have different shapes at different azimuthal angles instead of restricting the blade to a fixed static shape. In turn, this will positively reflect on the aerodynamic performance of VAWTs.

The concept of deformable blades have been implemented in many studies and showed its ability to improve the aerodynamic performance of VAWTs. Bouzaher et al. [19] investigated the use of flexible blades as an active flow control to improve the aerodynamic performance of VAWTs. The study was done numerically using Ansys Fluent on a two bladed VAWT with NACA0010 as the baseline airfoil. To perform the morphing motion, dynamic mesh technique was used in addition to a user defined function describing the morphing motion. A 38% improvement was reached by using this control strategy. Similarly, Leonczuk Minetto and Paraschivoiu [20] studied the use of morphing blade for VAWT. A computational fluid dynamics model was developed on STAR CCM+ Software and a combination of overset meshes and deforming meshes were used to perform the rotation of the turbine while the blades are morphing. Results indicated that applying blade morphing is able to prevent dynamic stall and an increase of 46.2% in power output was achieved. Moreover, MacPhee and Beyene [21] investigated the feasibility of using a flexible blade for VAWT that can adapt passively to flow conditions. The study was done numerically using OpenFOAM on a three-bladed NACA0015 VAWT by varying the blade's material flexibility. Results showed that an increase of 9.6% can be obtained by comparing the efficiency of the rigid and morphing rotor. In addition to that, Baghdadi et al. [22] performed a dynamic shape optimization for a VAWT blade to improve the turbine

output power. The study was based on CFD simulations of a three bladed VAWT with NACA0021 as baseline airfoil, and by using the Free-Form Deformation in addition to mesh morpher coupled with Torczon optimizer, optimal morphing of the blade was obtained to maximize the power output. Results of the 2D and 3D simulations showed a significant increase in power when compared to fixed-blade rotor. Furthermore, Wang et al. [23] performed a numerical study on the use of adaptive blades for VAWTs where the baseline airfoil used was NACA0015, and the degree of deformation of the blade was studied to get the deformation that yields the highest power coefficient at different turbine solidities and tip speed ratios (TSRs). In a later study, Wang et al. [1] developed a new blade design that can achieve active deformation for the leading and trailing edge of the blade. The study was done experimentally on NACA0012 airfoil by dividing the blade into five rotating segments, and with continuous deformation, different cambers can be achieved. Results showed that the aerodynamic performance of the blade can be improved by deforming the blade to a certain level where exceeding the critical camber level can affect the blade performance due to the friction resistance becoming a dominant factor.

Deformable blades has also been tested for hydrodynamic turbines and resulted in an improved performance. For instance, Zeiner-Gundersen [24] investigated the use of flexible foil for hydrodynamic vertical axis turbines by proposing a new blade design where the leading and trailing edges of the blade are fixed and the upper and lower surfaces are flexible. The experimental study was done in a controlled river environment and results showed that the flexible foils achieved higher power coefficient and better self-start at low inflow water velocities. Another study has been done by Hoerner et al. [25] on vertical axis water turbines where the effect of blade flexibility on the performance of the water turbine has been investigated. Results showed that a significant improvement was observed at low tip speed ratios when using highly flexible foils, whereas a minor advantage was found at high tip speed ratios. Hoerner et al. [25] concluded that the highly flexible foils become less effective as the tip speed ratio increases.

In summary, the proposed designs in these studies either require complicated control methods to deform the blade continuously at different azimuthal angles or require a lot of flexibility due to the morphing motion of the leading and trailing edges as proposed in some studies. To reduce the complexity of controlling the blades, the current study proposes a new design of flexible blades to be used in VAWTs which is inspired by Zeiner-Gundersen [24] research about the implementation of flexible foil for hydrodynamic vertical axis

4

turbines. This study includes the investigation of the use of flexible blades for VAWTs and the optimization of the design parameters of the blades using CFD simulations and design of experiments. Moreover, a comparison between the optimization results of the 2D CFD simulations and 3D CFD simulations is accomplished to determine the optimal design parameters of both 2D and 3D results. If an agreement between the 2D and 3D optimum conditions is proved, an important conclusion on the sufficiency of 2D simulations in the optimization processor is demonstrated. On the other hand, discrepancies in the optimum conditions between 2D and 3D simulations would prove that 2D optimization is not accurate. In addition to that, a detailed numerical study of the turbine aerodynamic performance based on this new design is done to compare between the rigid and flexible blade models' power coefficient and flow fields around the blades.

CHAPTER THREE

AIM, OBJECTIVES AND SCOPE

3.1 Aim

The aim of this research is to construct a two-dimensional and three-dimensional straight bladed vertical axis wind turbine. Ansys Fluent is used to study numerically the use of flexible blades and investigate their influence on the performance of the turbine and how the power coefficient cp can be improved with the new design.

3.2 Objectives

Ansys SpaceClaim is used to prepare the geometry of the turbine models, and Ansys Fluent is used to perform the numerical simulations using SST K omega and detached eddy simulation (DES) for the turbulence model of the 2D and 3D simulations respectively. Dynamic mesh is utilized to deform the blades based on a predefined function UDF. Design of experiments (DOE) is used to reduce the number of runs needed to optimize the geometry of the deformed blades.

3.3 Scope

The scope of this research is to study the use of flexible blades in VAWT and to optimize the geometry of the deformed blade to get the highest power coefficient. This is done through 2D and 3D numerical simulations. 2D simulations encounter some errors due to the neglected tip effects, so the same optimization is performed with 3D numerical simulations to compare the results of the 2D and 3D simulations. However, the effects of the struts and the rotor tower is neglected in this research.

CHAPTER FOUR

METHODOLOGY

4.1 Physical model

The Vertical axis wind turbine model used in this study is based on the rotor specifications of Li et al. [26] wind tunnel experiments. The straight-bladed H-rotor VAWT consists of two symmetrical NACA 0021 blades with a chord length of 265 mm and a blade pitch angle of 6 degrees. The diameter of the turbine is 2000 mm and the height of the blades is 1200 mm. As shown in Figure 1, the pitch angle β is the angle between the tangential line and the chord line of the blade. The freestream velocity is 8 m/s and the turbulence intensity of the wind tunnel is 0.5%. The turbine rotates clockwise with a tip speed ratio *TSR* ranging from 1.38 to 2.58 which results in an angular velocity ranging from 11.04 to 20.64 rad/s. All turbine specifications are detailed in Table 1.
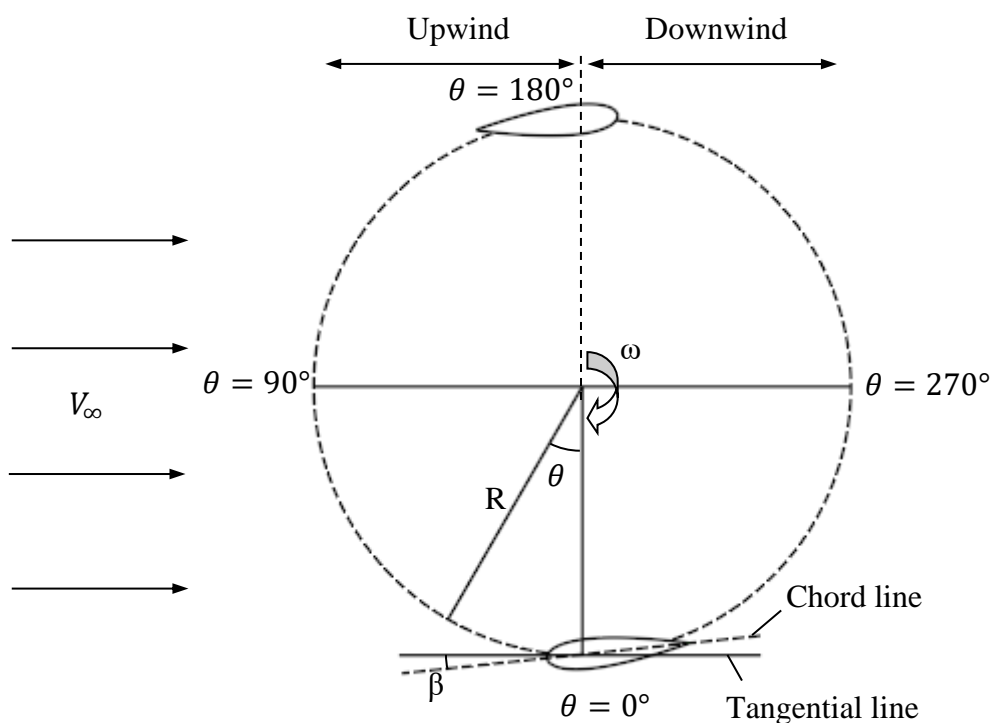
Figure 1: Defining Turbine Geometry

Table 1: Reference Turbine Specifications

Parameter	Specification
Airfoil	NACA0021
Turbine Diameter [m]	2
Chord Length [m]	0.265
Turbine Height [m]	1.2
Number of blades	2
Swept Area [m^2]	2.4
Pitch Angle [deg]	6
Solidity	0.265

4.2 Flexible Blade Design

The design of the flexible blade proposed in this study, inspired by Zeiner-Gundersen [24] design of flexible foil implemented for hydrodynamic vertical axis turbine is presented in Figure 2 and Figure 3. The blade is divided into two portions: a fixed portion and a flexible one as shown in Figure 2 where the main structure of the blade is preserved and a portion is allowed to deform.
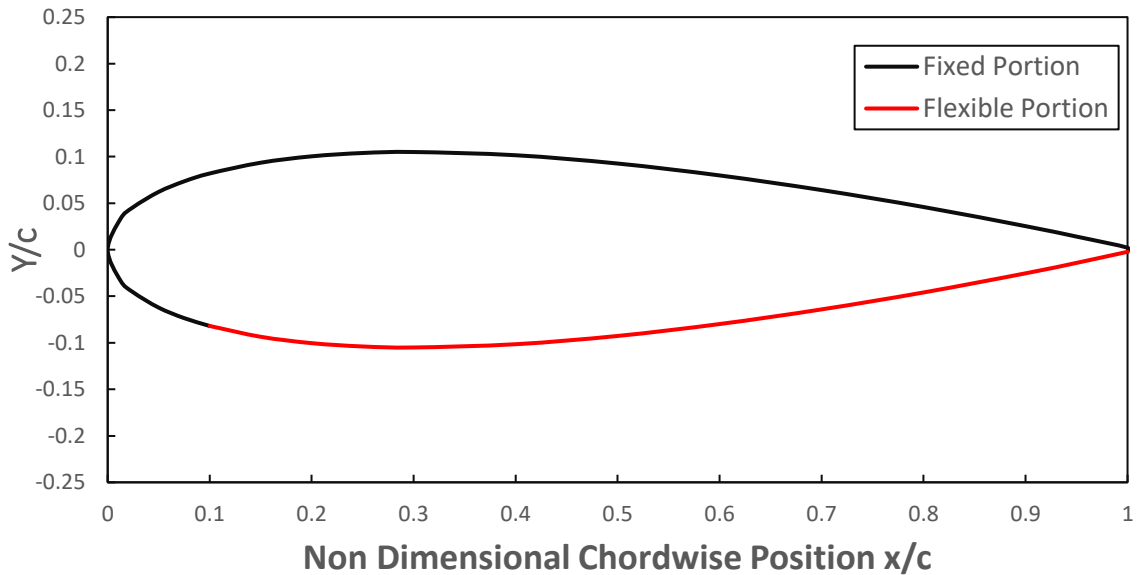
Figure 2: Flexible blade design showing the fixed and flexible portions

Figure 3 shows NACA0021 airfoil as the original blade, and the deformed blade that is used in the flexible blade model. The blade works during the rotation of the turbine based on two profiles, the deformed profile in the upwind side and the original profile in the

downwind side. A spline curve in Ansys SpaceClaim is used to define the deformed profile, and is constructed based on three main points: a point located at the trialing edge, a second point located at $X_d/2$ from the trailing edge and Y_d from the Original blade profile, and a third point located at X_d from the trailing edge as shown in Figure 3. The parameters which are varied and studied in this research are the chordwise flexible portion of the blade X_d and the amount of deformation from the original blade Y_d. An optimization of the turbine performance based on the aforementioned parameters was also performed.
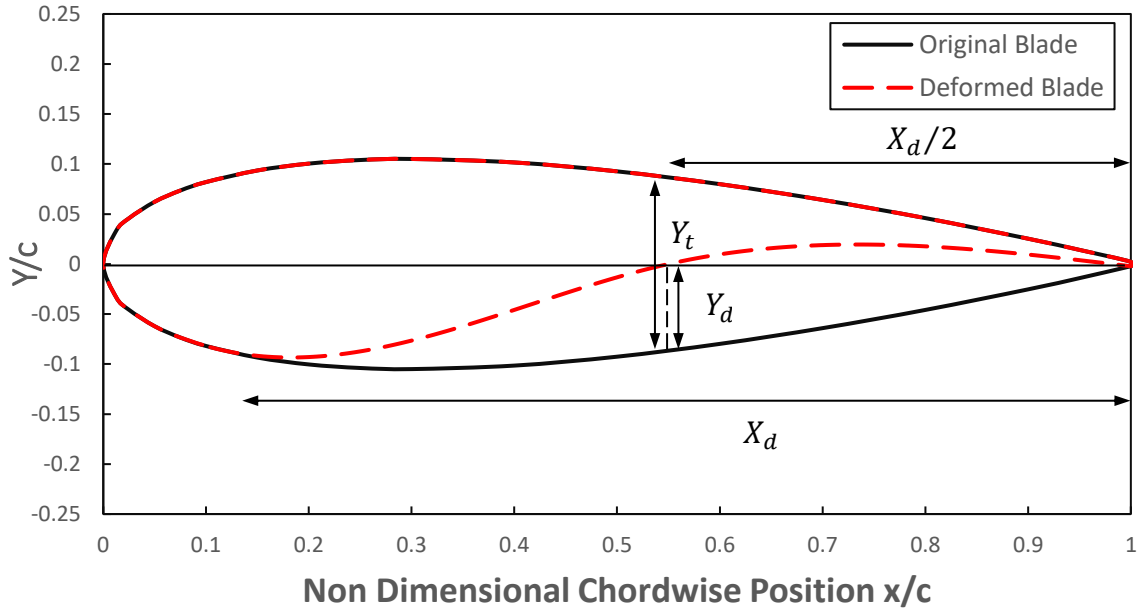
Figure 3: Design parameters of the flexible blade

X_d is normalized by the chord length c, and Y_d is normalized by the local thickness $Y_t|_{1-\frac{X_d}{2c}}$.

Where :

$$Y_t|_{1-\frac{X_d}{2c}} = 10 \times 0.21 \times [0.2969\sqrt{1-\frac{X_d}{2c}} - 0.1260\left(1-\frac{X_d}{2c}\right)$$
$$- 0.3516\left(1-\frac{X_d}{2c}\right)^2 + 0.2843\left(1-\frac{X_d}{2c}\right)^3$$
$$- 0.1015\left(1-\frac{X_d}{2c}\right)^4]$$

(1)

The ranges of variation of the two studied parameters are:

$$0.2 \leq \frac{X_d}{c} \leq 0.9 \quad \& \quad 0 \leq \frac{Y_d}{Y_t} \leq 0.5$$

9

4.3 Flexible Blade Turbine Model

The turbine with the proposed flexible blade will be working based on two blade profiles, the deformed blade in the upwind side and the original blade in the downwind side. The inward deformation of the blade starts at azimuth angle $\theta = 0°$ and ends at $\theta = 5°$ to have a smooth change from the original profile to the deformed one as shown in Figure 4. Between the azimuth angle $\theta = 5°$ and $\theta = 175°$, the deformed blade profile is kept unchanged. At $\theta = 175°$, the inward deformed blade will switch to the original blade profile over the course of 5 degrees to have a smooth deformation as shown in Figure 4. The turbine works based on the original blade profile in the downwind side. The same applies for the second blade with a 180 degrees shift.
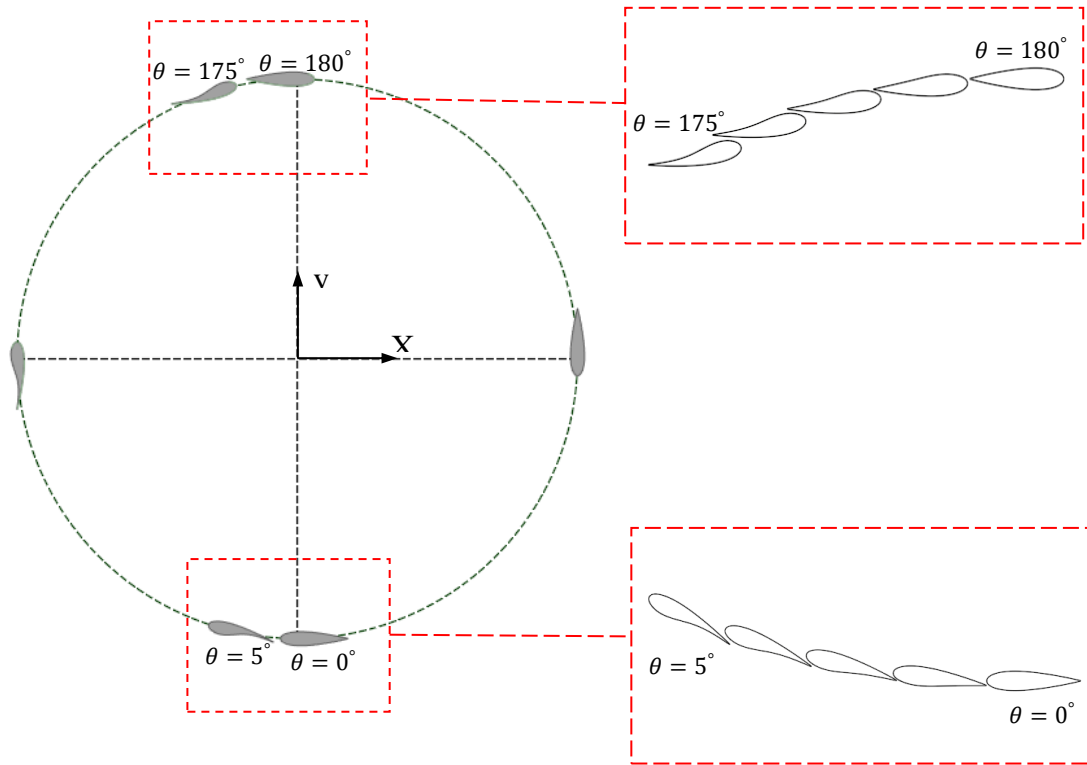
Figure 4: Flexible blade turbine model showing the azimuthal positions of blade deformation

4.4 User Defined Function (UDF)

A user defined function is a function that is written in C programming language and can be dynamically loaded with ANSYS Fluent solver to enhance its standard features and perform certain tasks. A UDF is used to perform the continuous deformation of the blade as

proposed in section 2.3, by controlling the nodes on the flexible surfaces of the blades. DEFINE_GRID_MOTION macro is utilized to have a full control over all the nodes and using this method, the position of the nodes can be updated at every timestep to reach the final deformed profile. MATLAB curve fitting tool is used to get an equation of the final deformed profile shown in Figure 3 and Fourier approximation with 6 terms is used to ensure a good fit with R-squared value of 1 and a root mean square error (RMSE) of 4.66×10^{-6} according to equation (2):

$$f(x) = a0 + a1\cos(wx) + b1\sin(wx) + a2\cos(2wx) + b2\sin(2wx) +$$
$$a3\cos(3wx) + b3\sin(3wx) + a4\cos(4wx) + b4\sin(4wx) + \qquad (2)$$
$$a5\cos(5wx) + b5\sin(5wx) + a6\cos(6wx) + b6\sin(6wx)$$

where $\quad 1 - X_d \leq x \leq 1$

$a0, a1, b1, a2, b2, a3, b3, a4, b4, a5, b5, a6, b6$, and w are the coefficients of the fitted deformed profile of the blade.

Twenty subframes are created to have a smooth deformation and to avoid large displacements of the nodes. These twenty subframes are created by linear interpolation between the final deformed shape and the original blade shape. Each frame updates the position of the nodes according to equation (2) taking into account the rotation needed at each timestep in addition to the deformation of the nodes based on a predefined array that contains all the coefficients of equation (2) as shown in equation (3):

$$Array = \begin{pmatrix} a0_{\theta=0.25} & \cdots & a0_{\theta=5} \\ \vdots & \ddots & \vdots \\ w_{\theta=0.25} & \cdots & w_{\theta=5} \end{pmatrix} \qquad (3)$$

4.5 Dynamic Mesh

A Dynamic mesh is usually used to simulate problems that include boundary motion, so it is used to perform the deformation needed during the rotation of the turbine using a compiled user defined function in ANSYS Fluent. Smoothing and remeshing schemes are used in setting up the dynamic mesh in order to maintain good elements quality and to avoid negative cell volume that can result if the mesh is moved too far during each timestep. Remeshing is only used for tetrahedral meshes in 3D and triangular meshes in 2D, so a mesh with triangular elements is used in this study. For the smoothing mesh method, diffusion method is capable to perform large deformations, and mesh smoothing parameters are set

as the following: diffusion function used is cell volume in order to avoid negative cell volume issues while deforming the blades, whereas the diffusion parameter and maximum number of iterations are kept as the default values set by Ansys fluent which are 1.5 and 50 respectively. In addition, dynamic mesh zones are defined to control the nodes positions on the surface of the blades. To do so, the deforming portion of the blade is defined as user defined zone where it follows the user defined function (UDF) compiled to Ansys Fluent, and the top and bottom surfaces of the blade are defined as deforming zones to adapt to the deformation of the user defined zone as shown in Figure 5.
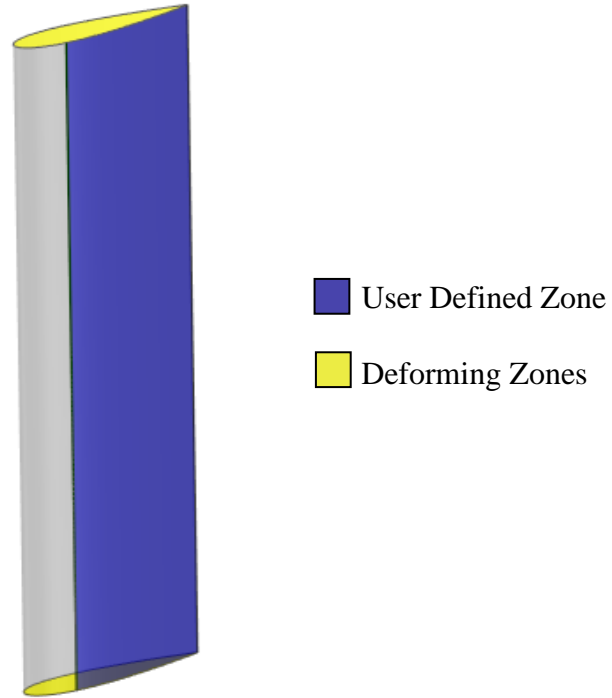
Figure 5: Dynamic mesh zones definition for the blade

4.6 Aerodynamic Parameters

The tip speed ratio (*TSR*) of a wind turbine is the ratio between the velocity at the tip of the blade and the freestream velocity and is denoted by λ:

$$\lambda = \frac{\omega . R}{V_\infty} \tag{4}$$

Where ω is the angular velocity in rad/s, R is the turbine radius in m and V_∞ is the wind freestream velocity in m/s.

The turbine performance is characterized by its power coefficient parameter *Cp*. Using Ansys Fluent, Moment coefficient *Cm* of the turbine can be determined and is calculated according to:

$$C_m = \frac{T}{0.5.\rho.A.R.(V_\infty)^2} \tag{5}$$

$$C_p = \frac{T.\omega}{0.5.\rho.A.(V_\infty)^3} = \lambda.C_m \tag{6}$$

Where *T* is the torque in N-m, ρ is the air density in Kg/m^3, *A* is the swept area in m^2, *R* is the turbine radius in m, and V_∞ is the freestream velocity in m/s.

4.7 Spatial Domain

Two main domains are considered to model the rotation of the turbine, namely rotating inner domain and stationary outer domain. The dimensions of these domains are based on the recommendations of Rezaeiha et al. [27] who provided guidelines for the minimum domain size that can be used for VAWT CFD simulations. All dimensions are represented as a function of turbine diameter D. The inner rotating domain is taken to be 1.5D and is located at 10D from the inlet and 15D from the outlet to allow full development of the wake. The stationary outer domain dimensions are 25D in length and 20D in width as shown in Figure 6. To connect the two considered domains, a mesh interface is used between the two zones to ensure the continuity of the flow and the pass of fluxes from one zone to the other. For the computational grid of the 3D simulations, similar dimensions to the 2D computational grid are used. The turbine blades' height is 1200 mm, and 200 mm gap is added between the blades' top and bottom surfaces and the rotating domain boundary to provide enough space for the produced vortices at the blade's tips. This results in a total height of 1600 mm for the inner domain. The outer domain height is taken to be 10 times the diameter of the turbine.
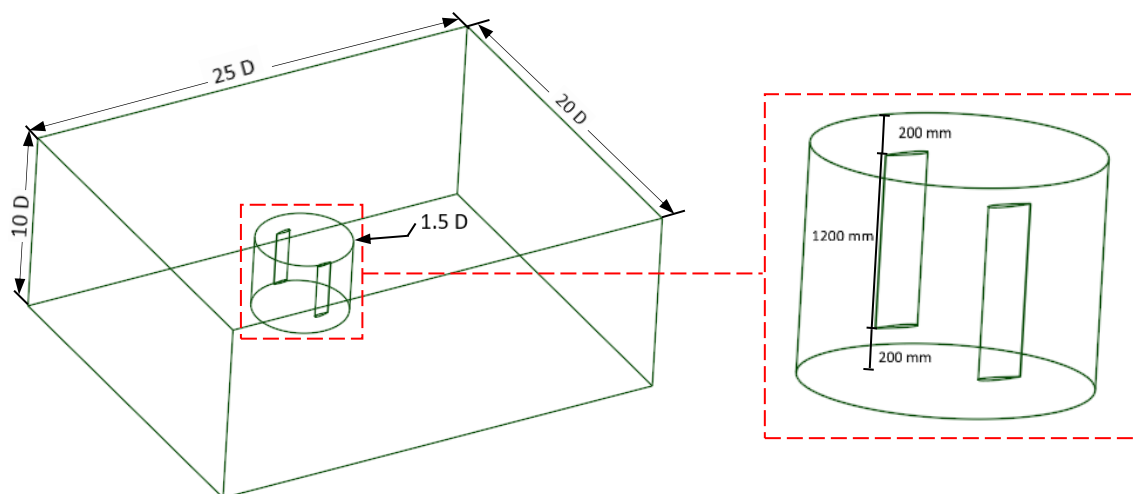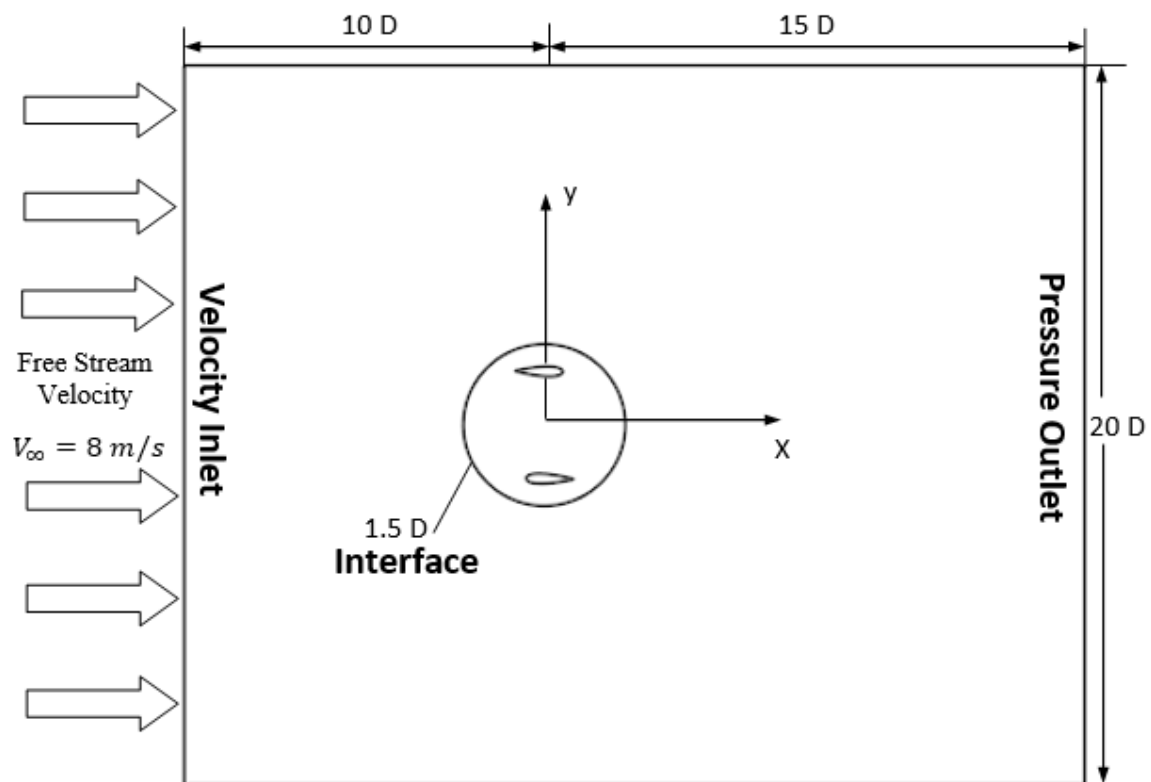
Figure 6: Computational Grid Schematic (not to scale)

4.8 Numerical Setup

The commercial software ANSYS Fluent was used to perform the numerical simulations. A transient pressure-based solver was used to solve the time-dependent Unsteady Reynolds-Averaged Navier Stokes (URANS) equations. The Pressure-Velocity coupling scheme used was coupled, and the spatial discretization gradient was set as least squares cell based. A second order upwind scheme was used for the pressure, momentum, turbulent kinetic energy and specific dissipation rate in addition to the second order implicit transient formulation. The turbulence model used for 2D simulations was SST K-omega which performs well with VAWT simulations that include flow separation [28] and for 3D simulations delayed detached eddy simulation (DDES) with SST K-omega as the RANS model are used to get accurate results and have lower computational time when compared to large eddy simulation (LES). The physical properties of the fluid used which is air are density $\rho = 1.225 \ kg/m^3$ and dynamic viscosity $\mu = 1.7894 \times 10^{-5} \ kg/m.s$. The sliding mesh technique was used for the inner rotating domain to simulate the VAWT motion. The boundary conditions are inlet velocity set as $V_\infty = 8 \ m/s$ at the inlet with 0.5% turbulence intensity and 18.55 mm turbulence length scale, pressure outlet set as 0 Pa gauge pressure at the outlet, mesh interface at the contact between the two zones (rotating and stationary), and no slip condition for the walls of the blades. To account for the height of the turbine in 2D simulations, depth used in reference values was changed to 1.2 m, and the swept area of the turbine was 2.4 m². The azimuthal increment used in the transient solver is $0.25°$ per timestep after a time independent study and the calculations use 20 iterations per timestep to ensure the convergence of the scaled residuals to 10^{-5}.

4.9 Computational Grid Mesh

4.9.1 2D Grid Mesh

(a)

(b)

(c)

(d)

(e)
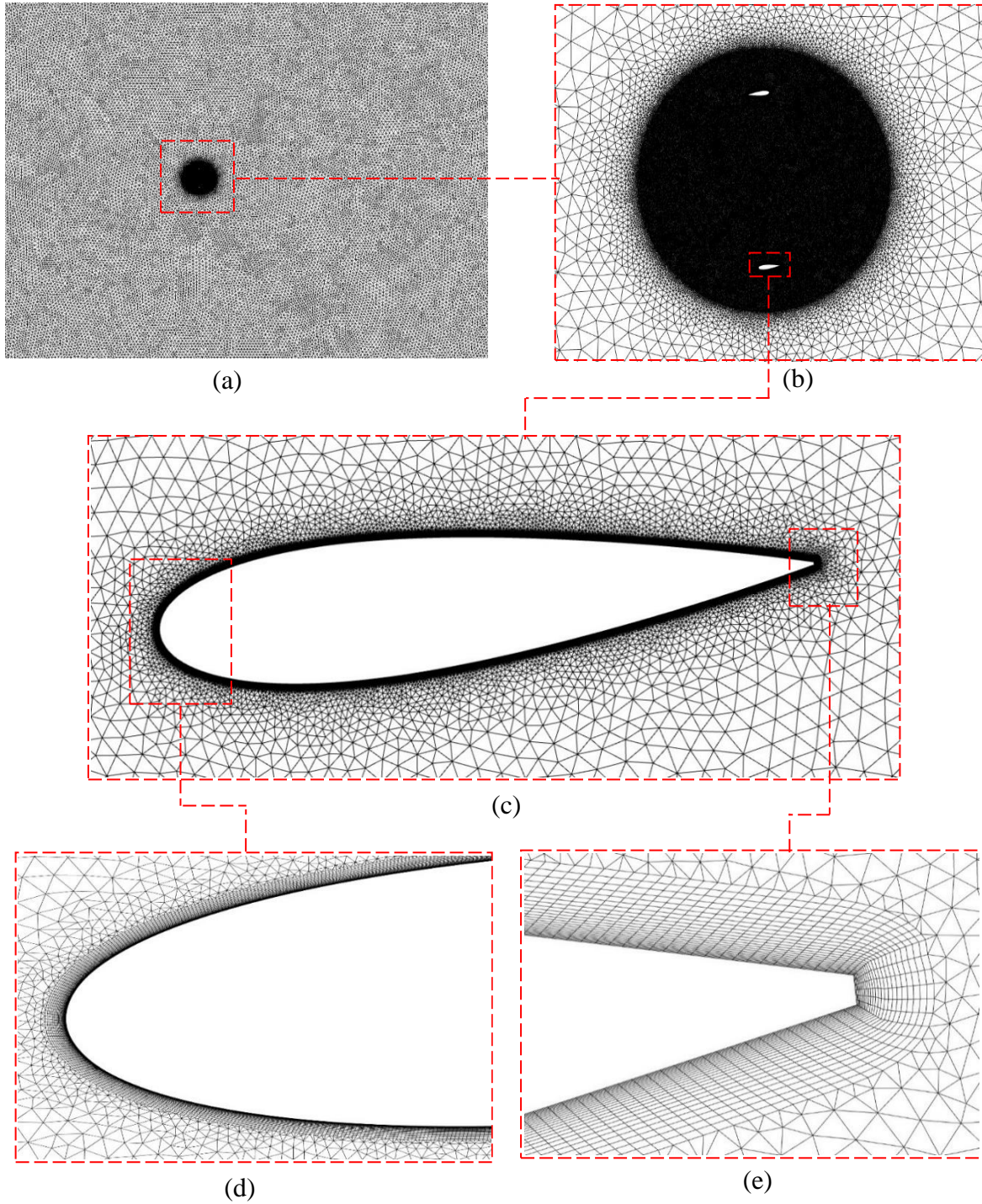
Figure 7: 2D Computational grid mesh distribution for (a) Outer domain, (b) Inner domain,(c) blade, (d) leading edge, and (e) Trailing edge

Figure 7 shows an unstructured triangular mesh used for the 2D turbine model. The inner rotating domain has approximately 80% of the total number of elements where a dense

mesh is needed around the turbine. The element size at the interface between the rotating and stationary domain is equal, and gradually increase in the stationary domain to 300 mm with a growth rate of 1.2. A fine mesh is used at the blades surfaces to accurately calculate the power coefficient of the wind turbine. The element size used at the blade surface is 0.5 mm with 25 inflation layers in which the first layer thickness is 0.03 mm and the growth rate is 1.1. This setup results in a y+<1.0.

2.9.2 3D Grid Mesh

(a)

(b)

(c)
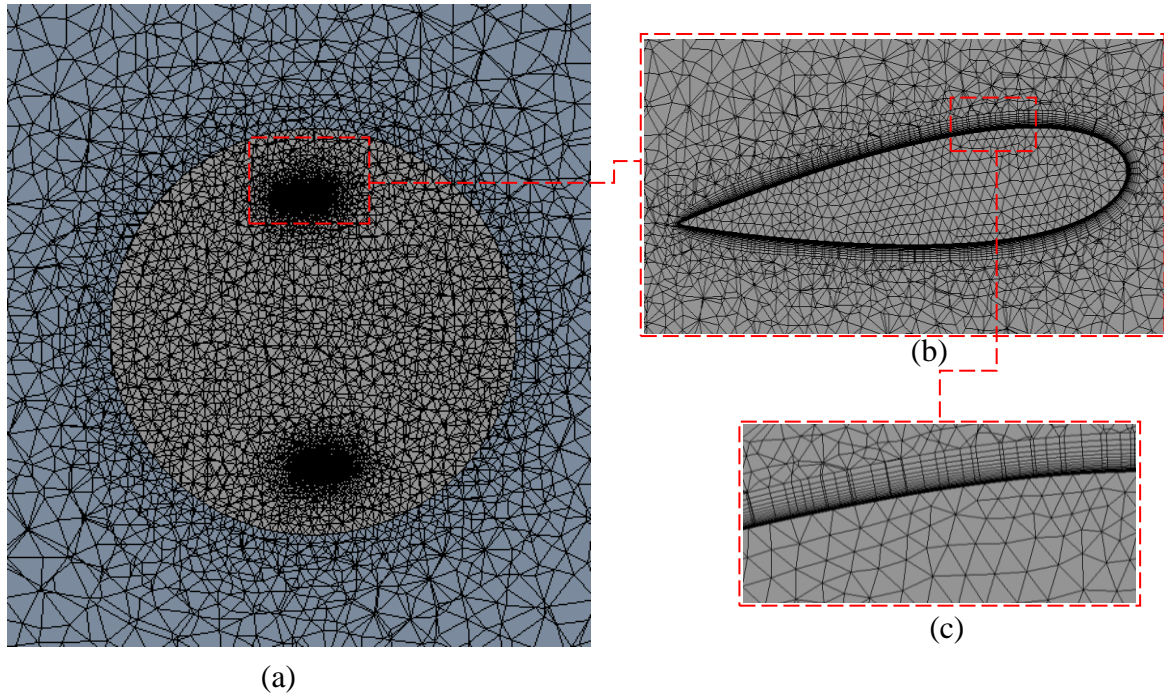
Figure 8: 3D Computational grid mesh distribution for (a) inner domain, (b) blade, (c) inflation layers near the blade

Figure 8 shows the mesh used for the 3D turbine model. A tetrahedral mesh is applied with higher density around the blades of the turbine. The inner domain element size is 100 mm, and the element size at the blade surfaces is 5 mm. 20 inflation layers are used with a growth rate of 1.2 and a first layer thickness of 0.045 mm, resulting in y+ ~ 1. Similar to the 2D mesh, the element size at the interface between the rotating and stationary domain was equal, and gradually increased to 2000 mm in the stationary domain with a growth rate of 1.2.

4.10 Convergence Criteria

The moment coefficient C_m calculated in ANSYS Fluent is monitored to ensure the convergence of the solution. The turbine is allowed to rotate 10 revolutions and the results of the last revolution was taken as the converged solution. Figure 9 shows the variation of moment coefficient as a function of azimuth angle, and it is clear that after 6 or 7 revolutions, a periodic solution was obtained. A convergence criterion represented by equation 7 is used,

$$Convergence\ Criterion = \frac{(Cm_{ave,n+1} - Cm_{ave,n})}{Cm_{ave,n}} < 1\% \qquad (7)$$

The difference between the moment coefficient at the 9th revolution $Cm_{ave,9}$ and the moment coefficient at the 10th revolution $Cm_{ave,10}$ is 0.27 % so calculations stop at the 10th revolution.
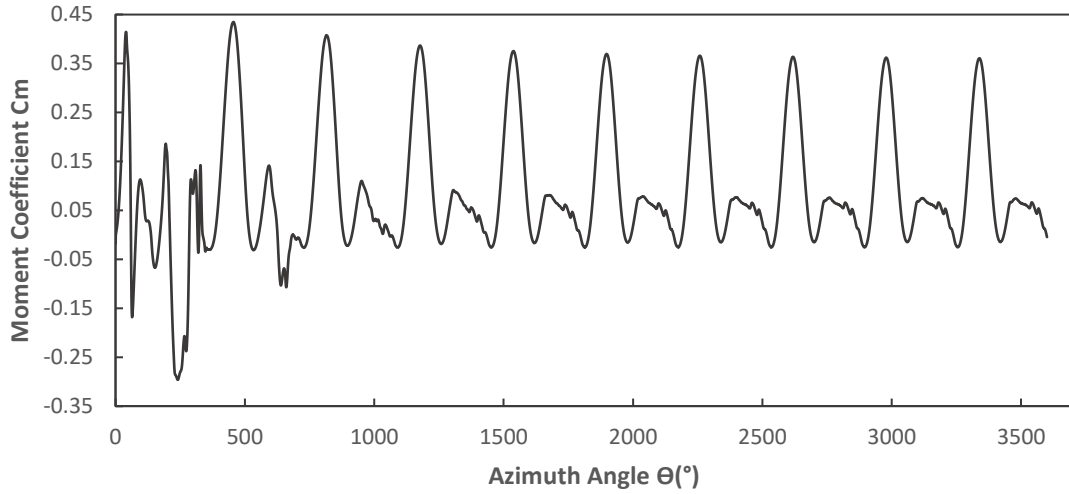
Figure 9: Moment Coefficient of 10 turbine revolutions at TSR=2.19

4.11 2D Model Verification

4.11.1 Grid Independent Study

To verify the CFD results obtained from ANSYS Fluent, a grid sensitivity study has been done to eliminate the mesh influence on the 2D model results. Four different meshes at $TSR = 2.19$ has been considered in this study where the element size at the airfoil surface, element size of the rotating inner domain in addition to the first layer thickness of the inflation layers were varied. The instantaneous moment coefficient C_m is plotted in Figure 10, and as shown the increase in the mesh density resulted in a mesh independent solution where the difference between mesh 3 whose number of elements is 270,000 elements and mesh 4 whose number of elements is 440,000 elements is less than 1%. So mesh 3 with the specified grid sizing in Table 2 is used in this research.
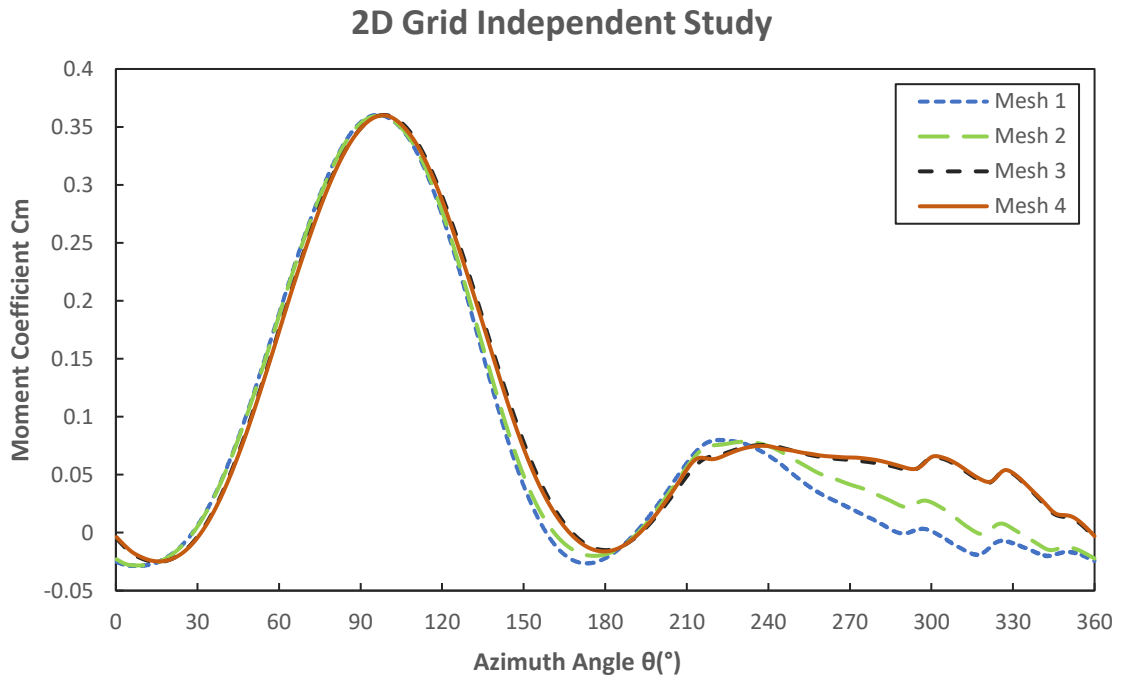
Figure 10: 2D Moment Coefficient of 4 grids at TSR=2.19

Table 2: 2D model 4 grids specifications

Grid	Number of Elements	Element Size (mm)		First layer Thickness (mm)
		Airfoil	Rotating Domain	
Mesh 1	101000	3	20	0.15
Mesh 2	143000	1.5	15	0.07
Mesh 3	270000	0.5	10	0.03
Mesh 4	440000	0.3	7.5	0.01

4.11.2 Time Independent Study

To study the effect of the azimuthal angle increment $d\theta$ (°) on the numerical results of 2D simulations, two different azimuthal increments are considered $d\theta = 0.1°$ and $d\theta = 0.25°$ at $TSR = 2.19$. As shown in Figure 11, the effect of decreasing the timestep size had no noticeable effect on the CFD results so $d\theta = 0.25°$ is used in this research.
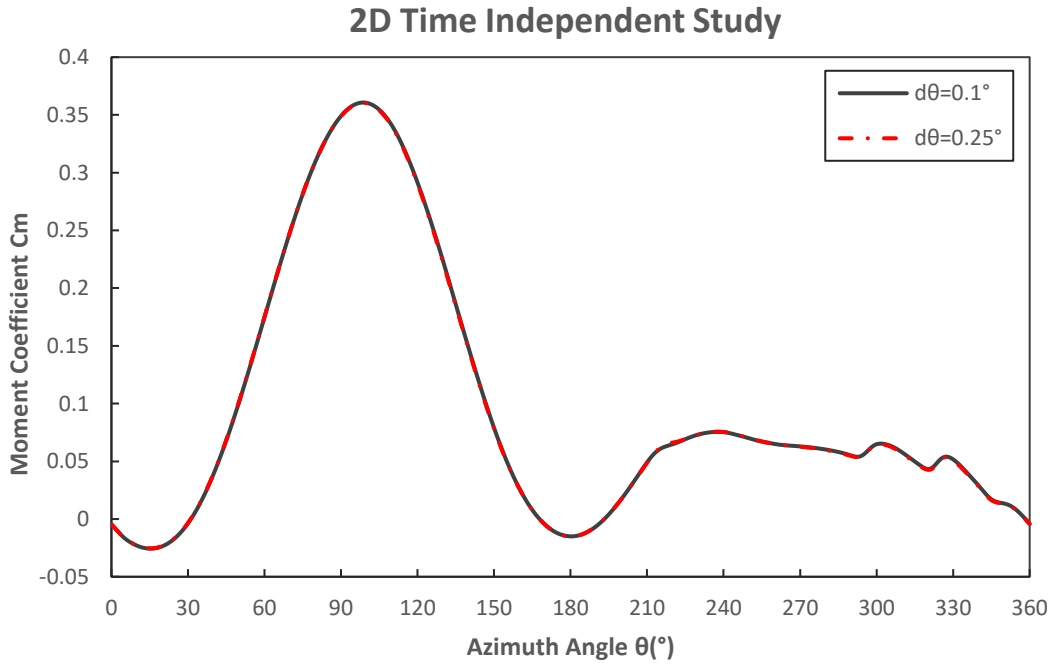
Figure 11: 2D Moment Coefficient at two different azimuthal increments at TSR=2.19

4.12 2D Model Validation

To validate the obtained results of the 2D CFD simulations, the pressure distribution at the blade surface for four different azimuthal angles are compared with the experimental results of Li et al. [26]. As shown in Figure 12, the comparison between CFD and experimental results at $\theta = 0°, \theta = 90°, \theta = 180°$ and $\theta = 270°$ at $TSR = 2.19$ shows acceptable agreement which validates the model considered in this study.
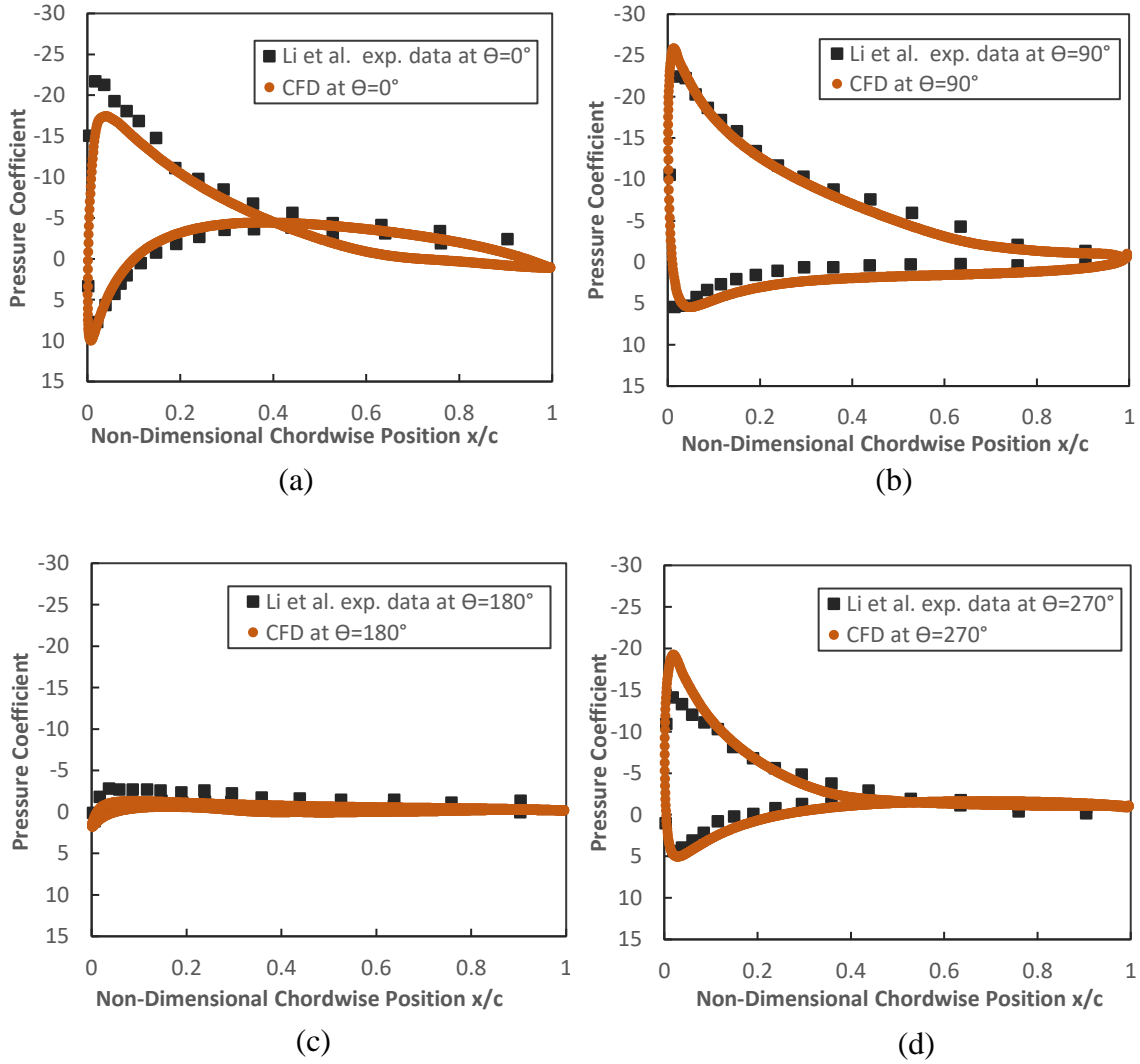
Figure 12: 2D Pressure Coefficient of CFD vs Li et al. data at (a) $\theta = 0°$, (b) $\theta = 90°$, (c) $\theta = 180°$ and (d) $\theta = 270°$ at $TSR = 2.19$

In addition to that, the 2D numerical results of Li et al. [29] were compared with the 2D CFD results of the current study, and as seen in Figure 13, a good agreement between the results was found when comparing the power coefficient of the VAWT at different tip speed ratios.
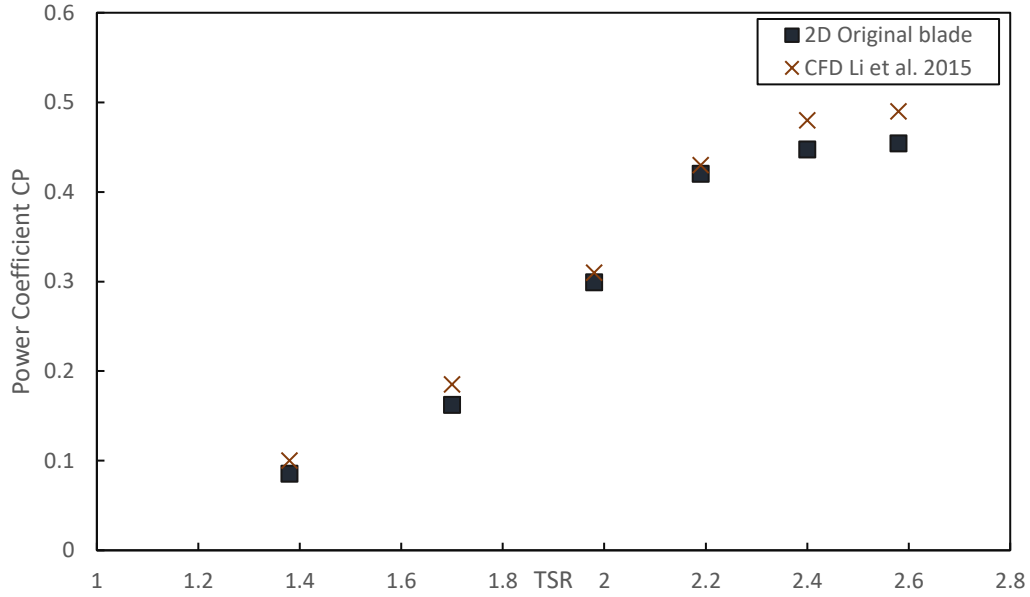
Figure 13: 2D CFD results vs 2D CFD results of Li et al. at different TSR values

4.13 3D Model Verification

4.13.1 Grid Independent Study
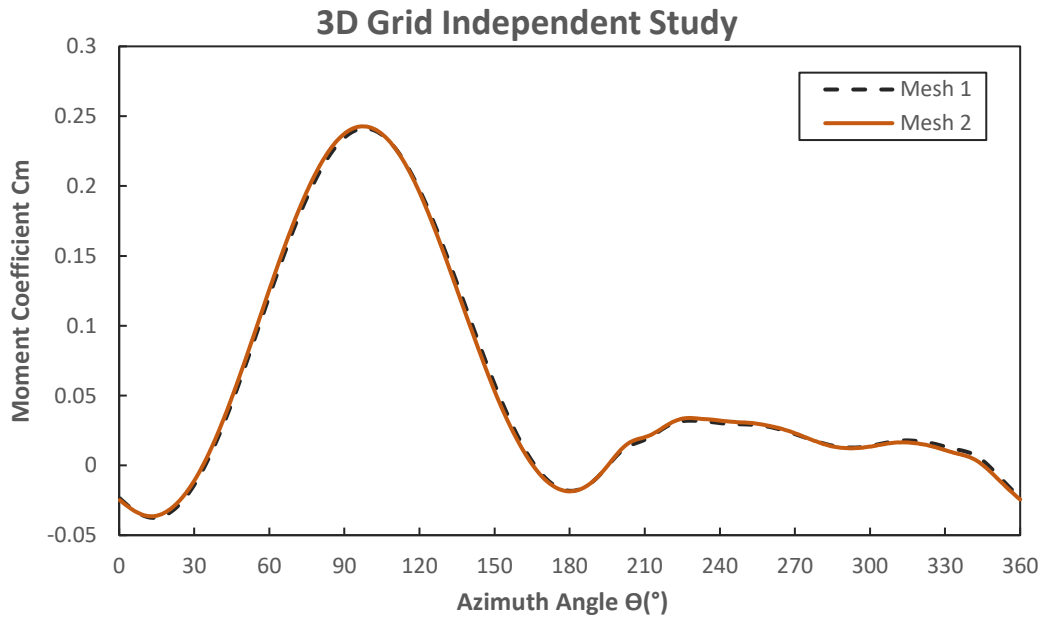
Figure 14: 3D Moment Coefficient of 2grids at TSR=2.58

A grid sensitivity study has been done for the 3D CFD simulations using two different meshes at $TSR = 2.58$ where the element size at the airfoil surface, and the first layer

thickness of the inflation layers were varied. Mesh 1 has 3.8 millions elements whereas Mesh 2 has 9.6 millions elements, and as seen in Figure 14, increasing the density of the mesh had minimal effect on the results, so Mesh 1 is used in this study.

4.13.2 Time Independent Study

Similar to the time sensitivity study of the 2D simulations, the effect of the azimuthal angle increment $d\theta\,(°)$ on the numerical results of 3D simulations has been studied by considering two azimuthal increments $d\theta = 0.1°$ and $d\theta = 0.25°$ at $TSR = 2.58$. As shown in Figure 15, the effect of decreasing the timestep size had no effect on the 3D CFD results so $d\theta = 0.25°$ is used in this research.

3D Time Independent Study
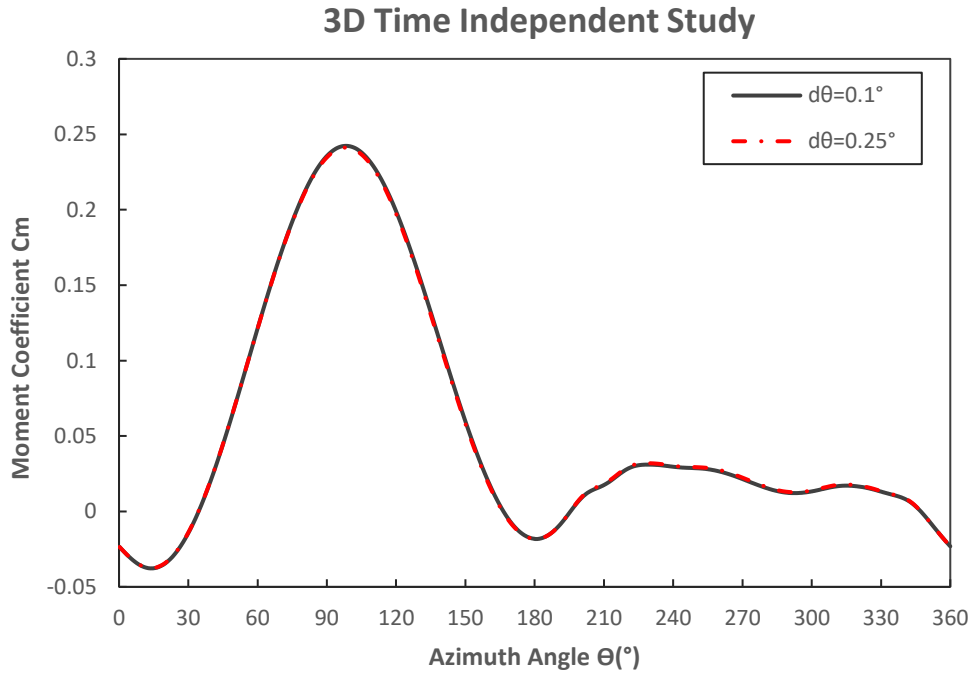
Figure 15: 3D Moment Coefficient at two different azimuthal increments at TSR=2.58

4.14 3D Model Validation

In order to validate the 3D CFD results, the pressure distribution at the blade surface for four different azimuthal angles are compared with the experimental results of Li et al. (2016). As shown in Figure 16, the comparison between CFD and experimental results at $\theta = 0°, \theta = 90°, \theta = 180°$ and $\theta = 270°$ at $TSR = 2.58$ shows good agreement which validates the model considered in this study.
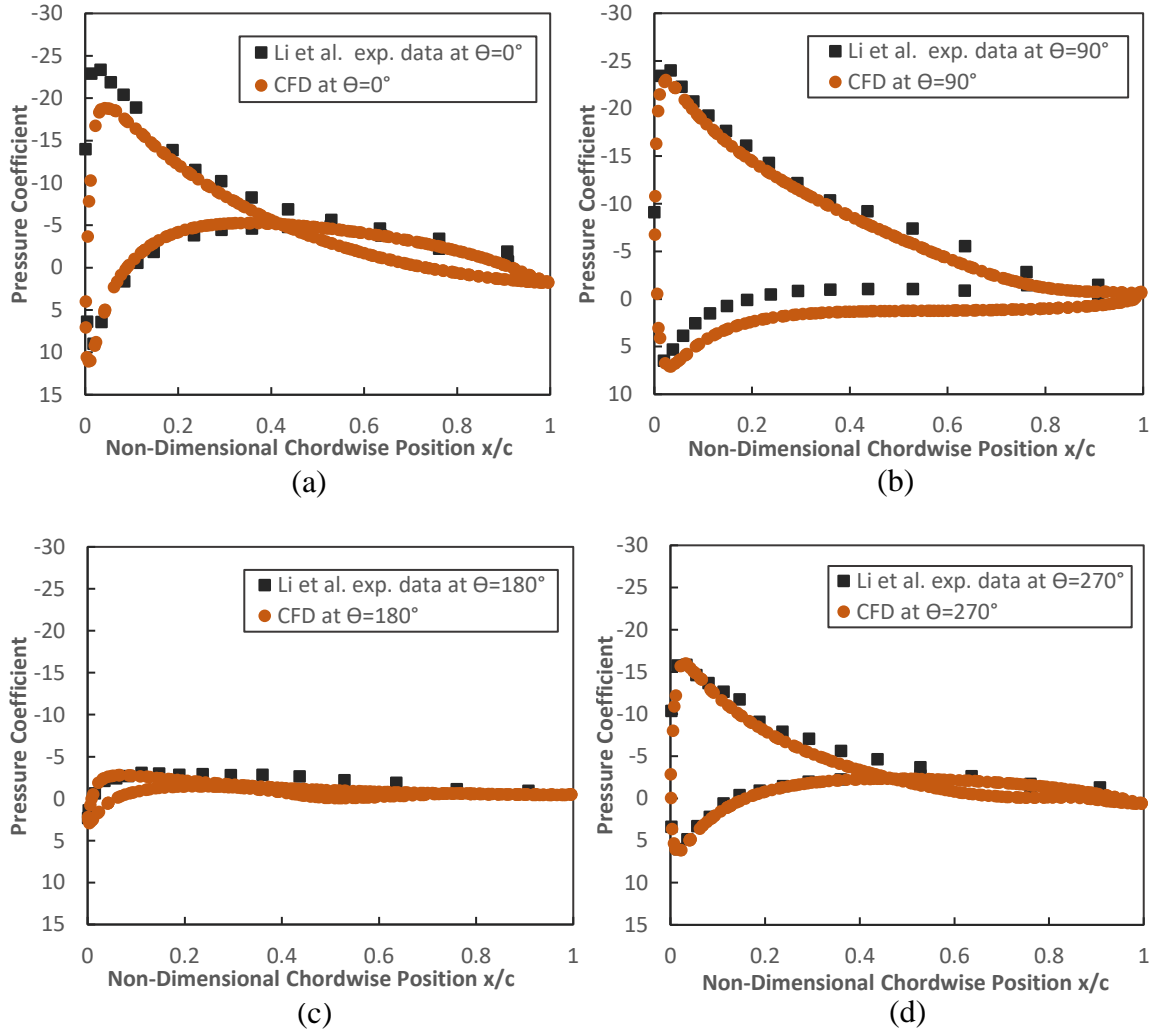
Figure 16: 3D Pressure Coefficient of 3D CFD vs Li et al. data at (a) $\theta = 0°$, (b) $\theta = 90°$, (c) $\theta = 180°$, and (d) $\theta = 270°$ at $TSR = 2.58$

CHAPTER FIVE

DESIGN OF EXPERIMENTS

5.1 A brief introduction to Design of Experiments

Design of experiments DOE is a systematic method that is widely used by scientists and engineers to study the relationship between input and output variables, and this method has been used in various fields of study to help in increasing the quality of the studied product or process resulting in a higher yield. As previously mentioned, DOE consists of input and output variables. Input variables are known as factors, and output variables are known as responses. The main objective of using DOE is to determine the effect of each factor on the response in addition to understanding the interaction of each factor's effect on the response in order to optimize the output response. Engineers had previously used design of experiments approach when optimizing a new design. Wind turbines for example have many parameters that require a large number of experiments or simulations to obtain an optimized design, so instead of performing the lengthy full factorial parametric study, a DOE approach can be used to reduce the number of experiments if it is an experimental study, or reduce the number of simulations if it is a numerical study. In both situations, this method will save time and it is less costly.

5.2 Literature Review about DOE

Design of experiments had been used in wind turbines studies. For example, Zhang et al. [30] designed a winglet for VAWT blades using orthogonal experimental design (OED) approach to optimize the six parameters used to define the configuration of the winglet. Results showed that the optimal winglet achieved a higher power coefficient at different tip speed ratios due to the reduced tip vortices effects. In addition, Wang et al. [31] applied a combination of 3D numerical simulations and Taguchi method to optimize the performance of a three-bladed VAWT using leading edge wavy serrations in addition to helical blade structure as the design parameters. Optimal results for the amplitude and wavelength of the serrations in addition to the optimal twist angle for the helical blade showed that power output was improved by 18.3%. Recently, Attie et al. [32] used numerical simulations and DOE method to optimize a single-slotted deflective flap at the trailing edge of the blade of

a VAWT. The optimal design parameters resulted in a 27% increase in output power compared to the baseline model. In the current study, a similar approach was considered to optimize the flexible blade parameters in order to improve the aerodynamic performance of the VAWT.

5.3 DOE approach, factors and levels

To get the optimal design parameters of the flexible blade, a Response Surface Methodology (RSM) is adopted in this study. RSM is an advanced DOE technique that is used to optimize the response by understanding the influence and interaction of the different factors. The factors and their levels that are considered in this study are based on a preliminary analysis in which different parameters are examined to decide the influential parameters and their range of variation.

Two design parameters for the flexible blade are considered: the chordwise flexible portion of the blade X_d and the amount of deformation from the original blade Y_d. These two parameters determine how the blade will be deformed dynamically in the proposed model. In addition to that, tip speed ratio TSR is another factor that is considered while designing the flexible blade. In short, three factors are used in the DOE Method, and a range of variability is required to study the effect of varying each factor. X_d/c varied between 0.2 and 0.9, the flexible portion did not exceed 90% of the chord in order to maintain the main structure of the leading edge. Y_d/Y_t varied between 0.05 and 0.5 where 0.05 is considered a very small deformation close to the original profile shape whereas 0.5 is the maximum deformation considered in this study, and tip speed ratio TSR varied between 1.38 and 2.58, to cover a wide range that involves low, moderate and high TSRs. Three levels for X_d and Y_d factors are considered, and four levels are considered for the TSR factor. Based on the preliminary analysis, it was observed that testing the different design parameters at various TSRs showed that the tip speed ratio is an influential factor on the other parameters to get the optimized response, so four levels of TSR are considered. These three variables with their corresponding levels are shown in Table 3:

Table 3: factors and levels considered in the DOE method

Levels	Factors		
	Chordwise Portion X_d/c	Deformation Y_d/Y_t	Tip Speed Ratio TSR
Level 1	0.2	0.05	1.38
Level 2	0.55	0.275	1.98
Level 3	0.9	0.5	2.19
Level 4	-	-	2.58

A face centered composite central design was adopted in this study to generate a well-balanced array that involve all the factors and their levels. The array consists of two central repetitive points and six axial points. A total of 20 combinations are generated and needed to model the response parameter. C_p/C_{po} is taken as the response parameter where C_p is the power coefficient of the turbine based on the corresponding factors and C_{po} is the power coefficient of the baseline turbine model at the corresponding TSR.

Table 4: Original power coefficient at different tip speed ratios

Tip Speed Ratio TSR	Original 2D Power Coefficient C_{po}	Original 3D Power Coefficient C_{po}
1.38	0.085	0.105
1.98	0.299	0.219
2.19	0.420	0.281
2.58	0.455	0.283

Table 4 shows the power coefficient of the original 2D and 3D turbine models, to be used in C_p/C_{po} response parameter under the objective of maximizing it. Four different

TSRs with their corresponding original power coefficient values are presented and these specific values are taken to cover the low, moderate, and high TSR regions.

5.4 DOE Array

As shown in Table 5, in order to determine the influence and significance of each factor, 20 runs are required to model the response C_p/C_{po} .

To analyze the data presented in Table 5, JMP Pro 16 Software was used to perform the statistical analysis procedure. Analysis of variance (ANOVA) was carried out to study the effect of each parameter on the response parameter and is detailed in the Results section. In addition, a fitted empirical model was obtained through regression modelling and a validation study was performed on the obtained model by testing different values of the parameters and checking how accurate the model predictions are. Moreover, an optimization process was carried out based on the empirical model where the optimal parameters of the flexible blade are determined at six different TSRs.

Table 5: DOE array showing the 20 generated combinations with their corresponding response

Run Number	Chordwise Portion X_d/c	Deformation Y_d/Y_t	Tip Speed Ratio TSR	2D Response C_p/C_{po}	3D Response C_p/C_{po}
1	0.2	0.05	1.38	1.0438	1.0053
2	0.9	0.05	1.38	1.0978	1.0573
3	0.2	0.5	1.38	1.2017	1.0841
4	0.9	0.5	1.38	1.6599	1.3240
5	0.55	0.275	1.38	1.2999	1.1635
6	0.2	0.275	1.98	1.1013	1.0676
7	0.55	0.05	1.98	1.0177	1.0425
8	0.55	0.275	1.98	1.2117	1.1467
9	0.55	0.275	1.98	1.2117	1.1467
10	0.55	0.5	1.98	1.2586	1.172
11	0.9	0.275	1.98	1.2586	1.2121
12	0.2	0.275	2.19	1.0445	1.0220
13	0.2	0.5	2.19	1.0441	1.0167
14	0.9	0.275	2.19	1.0902	1.0727
15	0.9	0.5	2.19	1.0899	1.0312
16	0.2	0.05	2.58	1.0028	0.9919
17	0.2	0.5	2.58	0.9966	0.9514
18	0.55	0.275	2.58	1.0084	0.9552
19	0.9	0.05	2.58	1.0037	0.9977
20	0.9	0.5	2.58	0.9809	0.8080

CHAPTER SIX

RESULTS AND DISCUSSION

6.1 DOE Results of 2D Simulations

6.1.1 Summary of the Fitted Model

Table 6: Summary of the fitted model based on 2D

Statistical Measure	Value
R-Squared	95.88%
Adjusted R-Squared	90.21%
Root Mean Square Error	0.0501

Table 6 shows that coefficient of determination (R-Squared) has a value of 0.9588 reflecting a good model fit of the collected data in Table 5. In addition to that, the Adjusted R-Squared which considers the impact of additional independent variables is also above 90% which also reflects the goodness of fit of the regression model. The root mean square error RSME presented in Table 6 shows the average difference between the values predicted by the model and the actual simulated values provided in Table 5, and a low RSME shows how close the observed points are to the fitted ones.

6.1.2 Analysis of Variance

In order to identify the significance of the considered factors in this DOE study, a three-way analysis of variance (ANOVA) is carried out. The individual effect of the three parameters, the two-way interaction between the parameters and reaching the analysis of the interaction of the three factors together was performed at 95% confidence intervals by analyzing the P-value of all interactions to determine their level of significance. A P-value is a statistical measurement that can show the statistical significance of the studied interactions, and a P-value of 0.05 or lower is considered significant for a 95% confidence level. Table 7 shows all the interactions with their corresponding degrees of freedom (DF), Sum of squares, F-Ratios, and P-values.

Table 7: Analysis of Variance (ANOVA)

Source	DF	Sum of Squares	F-Ratio	P-Value
A: X_d/c	1	0.01168194	4.6449	0.0633
B: Y_d/Y_t	1	0.08061931	32.0555	0.0005
C: TSR	1	0.19004041	75.5631	0.00002
AB	1	0.01622396	6.4509	0.0347
AC	1	0.03860948	15.3518	0.0044
BC	1	0.07705189	30.6371	0.0006
AA	1	0.00373978	1.487	0.2574
BB	1	0.00615223	2.4462	0.1564
CC	1	0.00020156	0.0801	0.7843
ABC	1	0.02464652	9.7999	0.014
ACC	1	0.00031632	0.1258	0.732

Table 7 shows, according to the analysis of variance (ANOVA), six considered interactions showed a high level of significance (P-Value<0.05). Tip Speed Ratio *TSR* has the most influential effect with a P-Value of 0.00002 which justifies considering four levels for this factor in the DOE array. The second influential factor is the deformation Y_d/Y_t with a P-Value 0.0005, followed by the interaction between Deformation and *TSR* with a P-Value of 0.0006. Also, the interaction between X_d/c and *TSR*, and X_d/c and Deformation showed a high significance with P-Values 0.0044 and 0.0347 respectively. It was also noticed that the three-way interaction between the factors has an important effect with a P-Value 0.014. On the other hand, the quadratic effect of the three factors showed low significance as their corresponding P-values are higher than 0.05.

6.1.3 Fitted Empirical Model

To model the dependent response parameter C_p/C_{po} as a function of the three factors considered, a multiple regression model based on the method of least squares is used to find the best fitting model for the observed data. The regression equation (8) is estimated by minimizing the sum of squared errors between the fitted model values and the collected data, and the least squared approach is used to estimate the values of the model coefficients. The equation that shows the relation between the response parameter C_p/C_{po} and the three factors X_d/c, Y_d/Y_t, and TSR is shown in equation (8):

$$
\begin{aligned}
\frac{C_p}{C_{po}} = 1.1793 &+ 0.0505 \times \left(\frac{X_d/c - 0.55}{0.35}\right) + 0.0847 \times \left(\frac{Y_d/Y_t - 0.275}{0.225}\right) \\
&- 0.1363 \times \left(\frac{TSR - 1.98}{0.6}\right) \\
&+ 0.0416 \times \left(\frac{X_d/c - 0.55}{0.35}\right) \times \left(\frac{Y_d/Y_t - 0.275}{0.225}\right) \\
&- 0.0687 \times \left(\frac{X_d/c - 0.55}{0.35}\right) \times \left(\frac{TSR - 1.98}{0.6}\right) \\
&- 0.0973 \times \left(\frac{Y_d/Y_t - 0.275}{0.225}\right) \times \left(\frac{TSR - 1.98}{0.6}\right) \\
&- 0.0324 \times \left(\frac{X_d/c - 0.55}{0.35}\right)^2 \\
&- 0.0415 \times \left(\frac{Y_d/Y_t - 0.275}{0.225}\right)^2 \\
&+ 0.0075 \times \left(\frac{TSR - 1.98}{0.6}\right)^2 \\
&- 0.055 \times \left(\frac{X_d/c - 0.55}{0.35}\right) \times \left(\frac{Y_d/Y_t - 0.275}{0.225}\right) \\
&\times \left(\frac{TSR - 1.98}{0.6}\right) \\
&+ 0.0107 \times \left(\frac{X_d/c - 0.55}{0.35}\right) \times \left(\frac{TSR - 1.98}{0.6}\right)^2
\end{aligned}
\tag{8}
$$

6.1.4 Fitted Model Validation

To validate the fitted regression model obtained by JMP Software, a validation study was done on the model by testing different combinations of values for the three considered factors through CFD numerical simulations, and comparing them with the predicted response value obtained from the model. The values were randomly chosen within the specified range of each variable, while making sure that they are different from the runs of

the DOE array. According to Table 8, the model is well predicting the response of the turbine as the different parameters are changing. Also, the error between the observed and predicted values is calculated according to:

$$Error = \left| \frac{(Predicted \; C_p/C_{po} - CFD \; C_p/C_{po})}{CFD \; C_p/C_{po}} \right| \times 100 \qquad (9)$$

It is clear that the error of all runs is lower than the root mean square error RSME (0.0501) of the model, which validates the obtained model to be used in predicting the turbine power coefficient improvement when varying the three considered factors.

Table 8: Comparison between 2D CFD response and fitted model predicted response at different combinations to validate the model

X_d/c	Y_d/Y_t	TSR	2D CFD C_p/C_{po}	Fitted Model Predicted C_p/C_{po}	Error (%)
0.9	0.5	2.4	1.03	1.04	1.49
0.7	0.21	1.38	1.30	1.30	0.01
0.2	0.19	2.19	1.04	1.06	1.57
0.5	0.27	1.38	1.29	1.30	1.01
0.2	0.19	2.4	1.02	1.04	1.33
0.4	0.27	1.7	1.15	1.19	3.48

6.1.5 Surface Plots at different TSRs

To understand the impact of each factor on the response parameter C_p/C_{po}, surface plots of the regression model are generated where the x and y axes show the chordwise portion X_d/c and deformation Y_d/Y_t whereas the z-axis shows the response parameter as shown in the figures below. Each figure has its own scale to make the surfaces clear, and the variation of the response C_p/C_{po} as a function of the design parameters of the flexible blade are shown at four different TSRs (1.38, 1.98, 2.19, 2.58). As shown in Figure 17, at low and moderate TSR values, large deformation ($X_d/c = 0.9$ & $Y_d/Y_t = 0.5$) for the flexible blade in the upwind side gives higher power coefficient when compared to the baseline model, whereas

at high tip speed ratio $TSR = 2.58$, moderate deformation for the blade gives the optimum power coefficient but with significantly lower improvement when compared to the performance of the flexible blade at low and moderate TSRs. This is clear in the surface plots below as the best performance of the flexible blade is at low tip speed ratio $TSR = 1.38$ with a 66% power improvement.
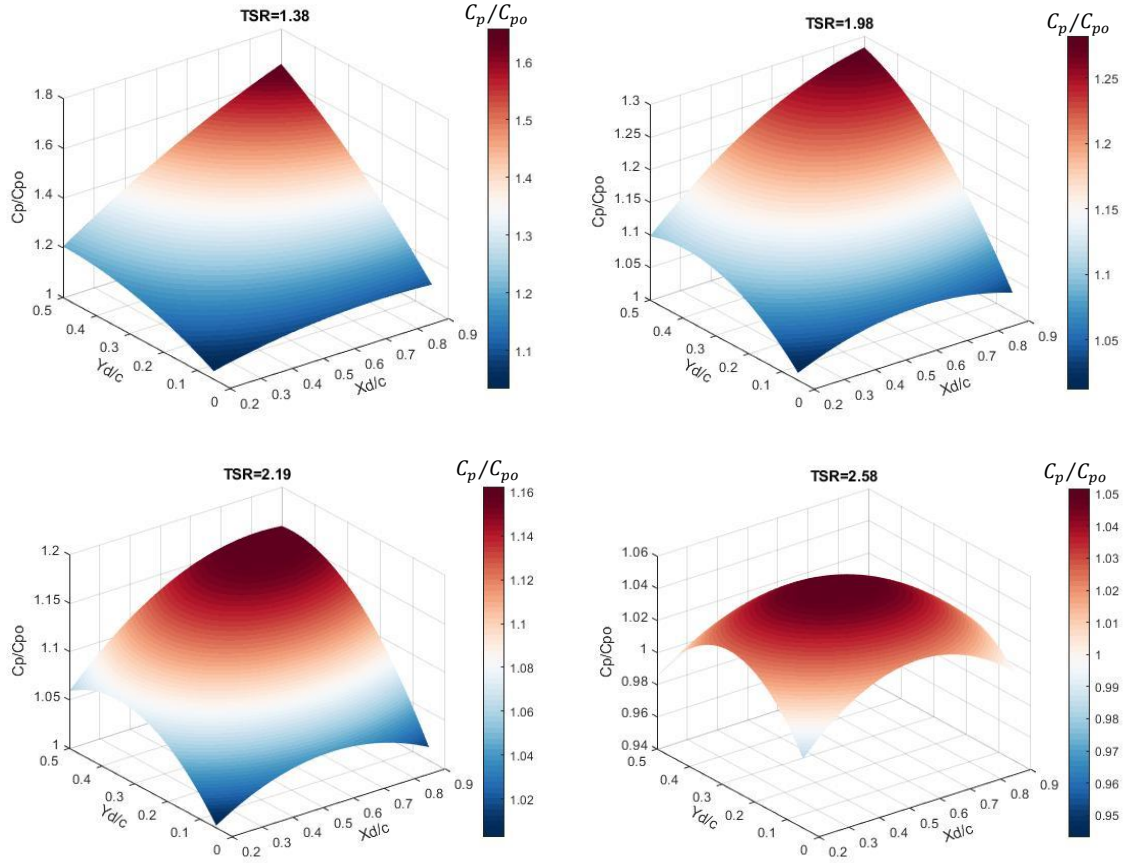
Figure 17: Surface plot of the response parameter Cp/Cpo as a function of Xd/c and Yd/Yt at TSR=1.38, 1.98, 2.19 and 2.58

6.1.6 Optimizing the turbine performance

To optimize the turbine power coefficient C_p, the fitted regression model that was previously validated is used to obtain the optimal design parameters of the flexible blades at different tip speed ratios *TSRs*. As shown in Table 9, the power coefficient of the flexible blades turbine is higher than the baseline turbine at all *TSR* values that cover the entire tested range. At low and moderate *TSR* values, namely *TSR* values between 1.38 and 2.19, $X_d/c = 0.9$ & $Y_d/Y_t = 0.5$ for the flexible blade gave the optimal power coefficient improvement, whereas moving to higher TSR values, a moderate deformation for the blade gave the optimal C_p. The highest power coefficient improvement was obtained at the lowest tip speed ratio $TSR = 1.38$ with a 66% increase and the turbine power improvement decreased gradually as *TSR* increased. That being said, the point with design parameters $X_d/c = 0.9$ & $Y_d/Y_t = 0.5$ will be called the global optimal point, whereas the other points will be known as the local optimal points.

Table 9: Optimal Design parameters of flexible blade at different TSR values

	Optimal Design Parameters		
TSR	X_d/c	Y_d/Y_t	Optimal C_p/C_{po}
1.38	0.9	0.5	1.658
1.7	0.9	0.5	1.453
1.98	0.9	0.5	1.282
2.19	0.9	0.5	1.159
2.4	0.6	0.3	1.089
2.58	0.55	0.275	1.051

The optimization of the design parameters at different *TSR* values was performed based on the predictive model obtained from the DOE approach used in this study. To further investigate the performance of the turbine at high tip speed ratios, a CFD study was performed, and the obtained results are shown in Table 10:

Table 10: Comparison between local optimal points and global optimal point at high TSR values

TSR	X_d/c	Y_d/Y_t	2D CFD C_p/C_{po}	Fitted Model Predicted C_p/C_{po}	Error (%)
2.4	0.6	0.3	1.033	1.089	5.4
	0.9	0.5	1.026	1.041	1.5
2.58	0.55	0.275	1.008	1.051	4.2
	0.9	0.5	0.981	0.943	3.8

Table 10 shows a comparison between the CFD numerical response and predicted model response C_p/C_{po} at the local optimal points obtained at each *TSR* value from the predictive model and at the global optimal point at low and moderate *TSR* values ($X_d/c = 0.9$ & $Y_d/Y_t = 0.5$). Again, CFD results validate the predictive model with a maximum error of about 5% at some point which is stated by the root mean square error RMSE of this regression model. Analyzing the obtained results shows that the turbine power coefficient improvement C_p/C_{po} at $TSR = 2.4$ slightly decreases when moving from the local optimal point ($X_d/c = 0.6$ & $Y_d/Y_t = 0.3$) to the global optimal point ($X_d/c = 0.9$ & $Y_d/Y_t = 0.5$). Similarly, at $TSR = 2.58$, a slight decrease was obtained when working with the global optimal point which is clear when analyzing the CFD observed results.

These obtained results show that the flexible blades turbine model works better at low and moderate tip speed ratios whereas when moving to higher *TSR* values, the improvement was small at different design parameter combinations for the flexible blade as shown in Table 10. Therefore, based on the DOE analysis of the 2D CFD results, it can be suggested to use the flexible blade model at low and moderate *TSR* values while at high TSRs, no significant improvement was noticed.

6.2 DOE Results of 3D Simulations

6.2.1 Summary of the Fitted Model

Table 11: Summary of the fitted model based on 3D

Statistical Measure	Value
R-Squared	95.94%
Adjusted R-Squared	90.37%
Root Mean Square Error	0.0344

Similar to 2D analysis, coefficient of determination (R-Squared) and the Adjusted R-Squared shown in Table 11 have high values showing the goodness of fit of the regression model. Also, the root mean square error RSME has a low value.

6.2.2 Analysis of Variance

In order to identify the significance of the considered factors in the DOE study based on the 3D CFD results, a three-way analysis of variance (ANOVA) is carried out. Similarly, the individual effect of the three parameters, the two way interaction between the parameters and reaching to the analysis of the interaction of the three factors together was performed at 95% confidence intervals by analyzing the P-value of all interactions to determine their level of significance. Table 12 shows all the interactions with their corresponding degrees of freedom (DF), Sum of squares, F-Ratios, and P-values.

Table 12: Analysis of Variance

Source	DF	Sum of Squares	F-Ratio	P-Value
A: X_d/c	1	0.01440673	12.1493	0.0083
B: Y_d/Y_t	1	0.00500339	4.2194	0.0740
C: TSR	1	0.09423230	79.4669	0.00002
AB	1	0.00003468	0.0292	0.8685
AC	1	0.02502610	21.1047	0.0018
BC	1	0.04390357	37.0243	0.0003
AA	1	0.00149876	1.2639	0.2935
BB	1	0.00268219	2.2619	0.1710
CC	1	0.01434638	12.0984	0.0083
ABC	1	0.01518859	12.8087	0.0072
ACC	1	0.00384611	3.2435	0.1094

According to the analysis of variance (ANOVA) of the DOE results based on the 3D CFD simulations shown in Table 12, six considered interactions also showed a high level of significance (P-Value<0.05). Similar to the 2D Analysis, Tip Speed Ratio *TSR* has the most influential effect with a P-Value of 0.00002. The second influential factor is the interaction between deformation Y_d/Y_t and *TSR* with a P-Value 0.0003, followed by the interaction between X_d/c and *TSR* with a P-Value of 0.0018. Also, X_d/c showed a high significance with P-Values 0.0083. It was also noticed that similar to the 2D analysis, the three way interaction between the factors has an important effect with a P-Value 0.0072. On the other hand, the quadratic effect of the tip speed ratio *TSR* showed a high significance which contradicts the results obtained from the DOE analysis based on the 2D results. Finally, the quadratic effect of the two other factors showed low significance as their corresponding P-values are higher than 0.05.

6.2.3 Fitted Empirical Model

JMP Software was also used to get a model based on 3D CFD results. The dependent response parameter C_p/C_{po} was also modelled as function of the three factors considered and a multiple regression model is used to find the best fitting model for the observed data. The equation that shows the relation between the response parameter C_p/C_{po} and the three factors X_d/c , Y_d/Y_t, and TSR is:

$$
\begin{aligned}
\frac{C_p}{C_{po}} = 1.1349 &+ 0.0560 \times \left(\frac{X_d/c - 0.55}{0.35}\right) + 0.0211 \times \left(\frac{Y_d/Y_t - 0.275}{0.225}\right) \\
&- 0.0960 \times \left(\frac{TSR - 1.98}{0.6}\right) \\
&+ 0.0019 \times \left(\frac{X_d/c - 0.55}{0.35}\right) \times \left(\frac{Y_d/Y_t - 0.275}{0.225}\right) \\
&- 0.0553 \times \left(\frac{X_d/c - 0.55}{0.35}\right) \times \left(\frac{TSR - 1.98}{0.6}\right) \\
&- 0.0734 \times \left(\frac{Y_d/Y_t - 0.275}{0.225}\right) \times \left(\frac{TSR - 1.98}{0.6}\right) \\
&- 0.0205 \times \left(\frac{X_d/c - 0.55}{0.35}\right)^2 \\
&- 0.0274 \times \left(\frac{Y_d/Y_t - 0.275}{0.225}\right)^2 \\
&- 0.0637 \times \left(\frac{TSR - 1.98}{0.6}\right)^2 \\
&- 0.0432 \times \left(\frac{X_d/c - 0.55}{0.35}\right) \times \left(\frac{Y_d/Y_t - 0.275}{0.225}\right) \\
&\quad \times \left(\frac{TSR - 1.98}{0.6}\right) \\
&- 0.0373 \times \left(\frac{X_d/c - 0.55}{0.35}\right) \times \left(\frac{TSR - 1.98}{0.6}\right)^2
\end{aligned}
\tag{10}
$$

6.2.4 Fitted Model Validation

Similarly, to validate the fitted regression model obtained by JMP Software, a validation study was done on the model by testing the same combinations of values used for the validation of the model based on 2D CFD results.

Table 13: Comparison between 3D CFD observed response and fitted model predicted response at different combinations to validate the model

X_d/c	Y_d/Y_t	TSR	3D CFD C_p/C_{po}	Fitted Model Predicted C_p/C_{po}	Error (%)
0.9	0.5	2.4	0.905	0.928	2.54
0.7	0.21	1.38	1.17	1.16	1.01
0.2	0.19	2.19	1.02	1.03	1
0.5	0.27	1.38	1.14	1.15	1
0.2	0.19	2.4	0.991	1.014	2.32
0.4	0.27	1.7	1.10	1.13	2.5

6.2.5 Surface Plots at different TSRs

Figure 18 shows the surface plots of the response parameter C_p/C_{po} as a function of the chordwise portion X_d/c and deformation Y_d/Y_t. Similarly, each figure has its own scale to make the surfaces clear, and the variation of the response C_p/C_{po} as a function of varying the design parameters of the flexible blade are shown at three different TSRs (1.38, 1.98, 2.19). As shown in Figure 18, at low *TSR* values, large deformation ($X_d/c = 0.9$ & $Y_d/Y_t = 0.5$) for the flexible blade in the upwind side gives higher power coefficient when compared to the baseline model, whereas at moderate *TSR* values, moderate deformation Y_d/Y_t for the blade gives the optimum power coefficient. At high tip speed ratios, flexible blade did not improve the turbine performance.
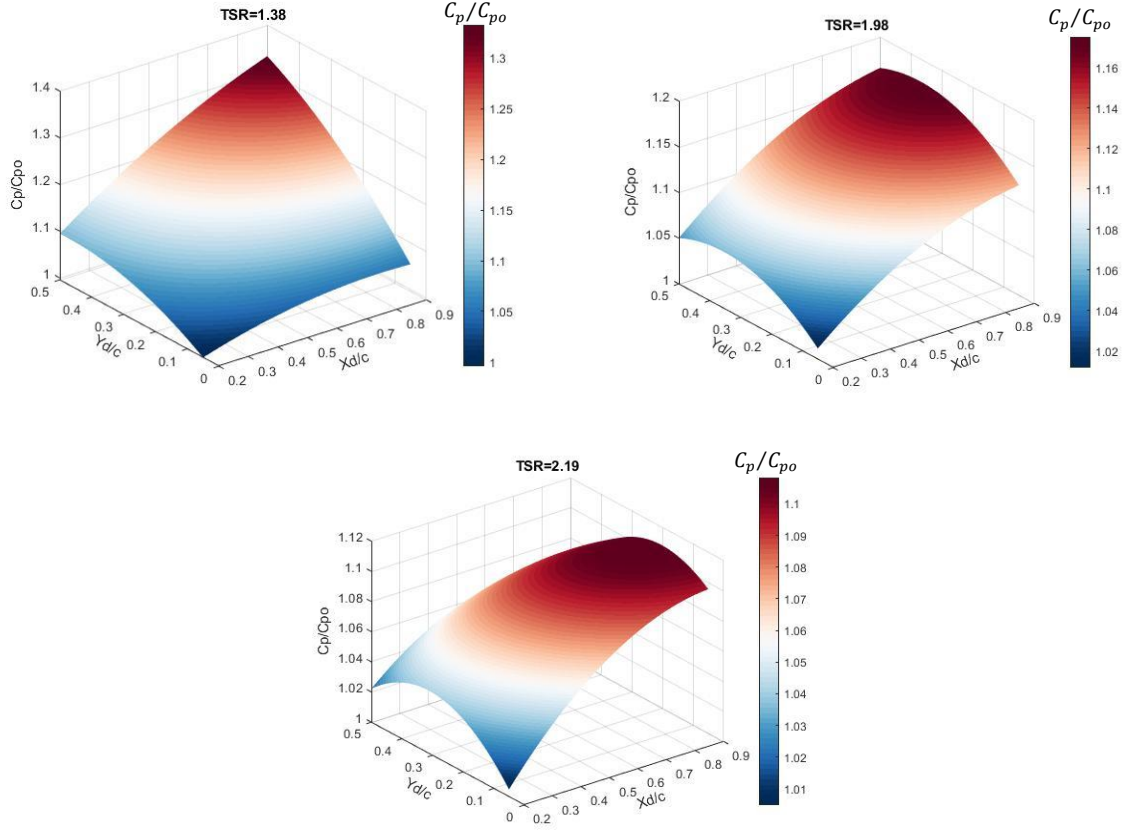
Figure 18: Surface plots of the response parameter Cp/Cpo as a function of Xd/c and Yd/Yt at TSR=1.38, 1.98 and 2.19

6.2.6 Optimizing the turbine performance

Similar to the 2D analysis, JMP Software was used to obtain the optimal design parameters of the flexible blades at different tip speed ratios *TSR*. As shown in Table 14, the power coefficient of the flexible blades turbine is higher than the baseline turbine at low and moderate *TSR* values whereas no optimum point was found at high *TSR (TSR=2.58)*. At low TSRs, namely *TSR* values between 1.38 and 1.7, $X_d/c = 0.9$ & $Y_d/Y_t = 0.5$ for the flexible blade gave the optimal power coefficient improvement, whereas moving into moderate TSR values, a moderate deformation for the blade gave the optimal C_p which is slightly different from the DOE results of 2D CFD data. The highest power coefficient improvement was obtained at the low tip speed ratio $TSR = 1.38$ with a 33% increase and the turbine power improvement decreased gradually as *TSR* increased similar to the DOE results of the 2D CFD simulations.

Table 14: Optimal Design Parameters based on 3D Analysis

	Optimal Design Parameters		
TSR	X_d/c	Y_d/Y_t	Optimal C_p/C_{po}
1.38	0.9	0.5	1.33
1.7	0.9	0.5	1.27
1.98	0.9	0.4	1.175
2.19	0.9	0.275	1.10
2.4	0.6	0.2	1.04
2.58	0	0	1

6.2.7 Power Coefficient vs TSR

Figure 19 shows the baseline turbine model's power coefficient in addition to the power coefficient of the flexible blade turbine model at the optimum points determined by the DOE study. As shown, using these design parameters of the flexible blade at different *TSR* values improve the aerodynamic performance of the wind turbine with a decrease in the power coefficient improvement as the tip speed ratio (*TSR*) increases. It is also noticeable that 2D and 3D results show a similar pattern in terms of the effectiveness of using flexible blades for VAWTs at low and moderate tip speed ratios whereas it is less effective at high tip speed ratios.
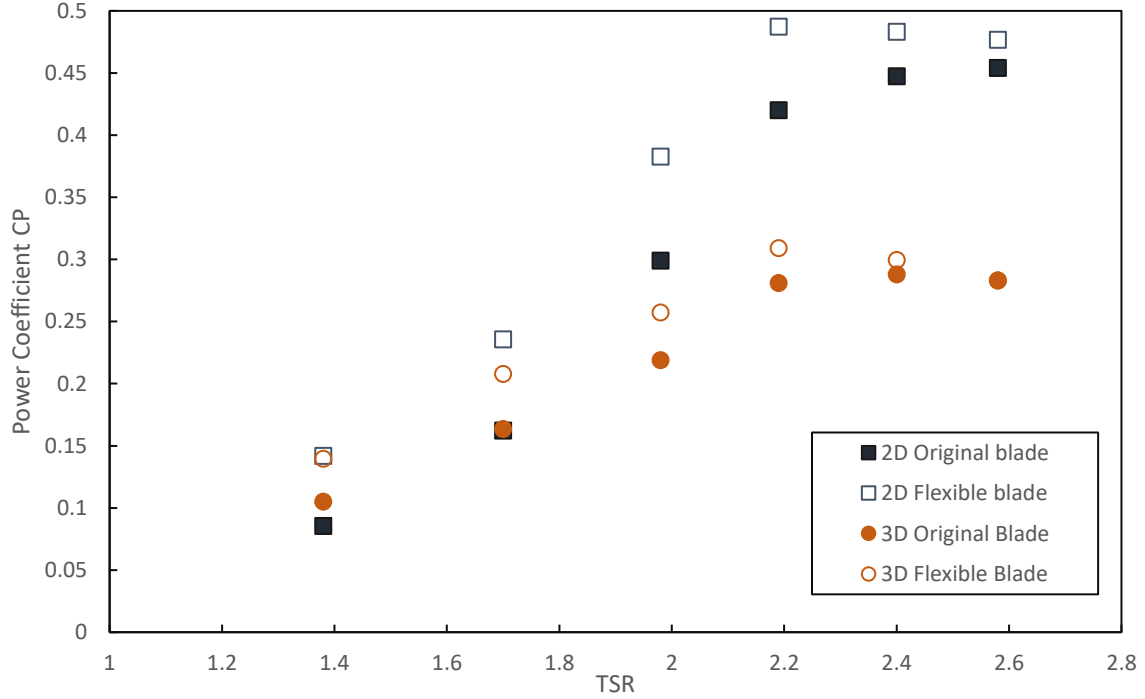
Figure 19: Power coefficient of original blade turbine model vs flexible blade turbine model at optimum points of DOE results

6.3 CFD Results

6.3.1 2D Instantaneous Moment Coefficient of One Blade

Figure 20 shows the instantaneous moment coefficient of one full revolution of the VAWT for both wind turbine with the original blade and wind turbine with the optimized flexible blade at $TSR = 1.38$. As seen in Figure 20, the new blade design improved the turbine performance when applied in the upwind side, and when the blade gets back to its original shape during the downwind side, it is seen that the curve follows the original blade moment coefficient curve with a noticeable variation after azimuthal position $\theta = 270°$ where the downstream wake generated by the deformed blade in the upwind side affects the flow around the downwind side blade leading to a better aerodynamic performance between $270° < \theta < 310°$ and a reduced performance between $310° < \theta < 360°$.
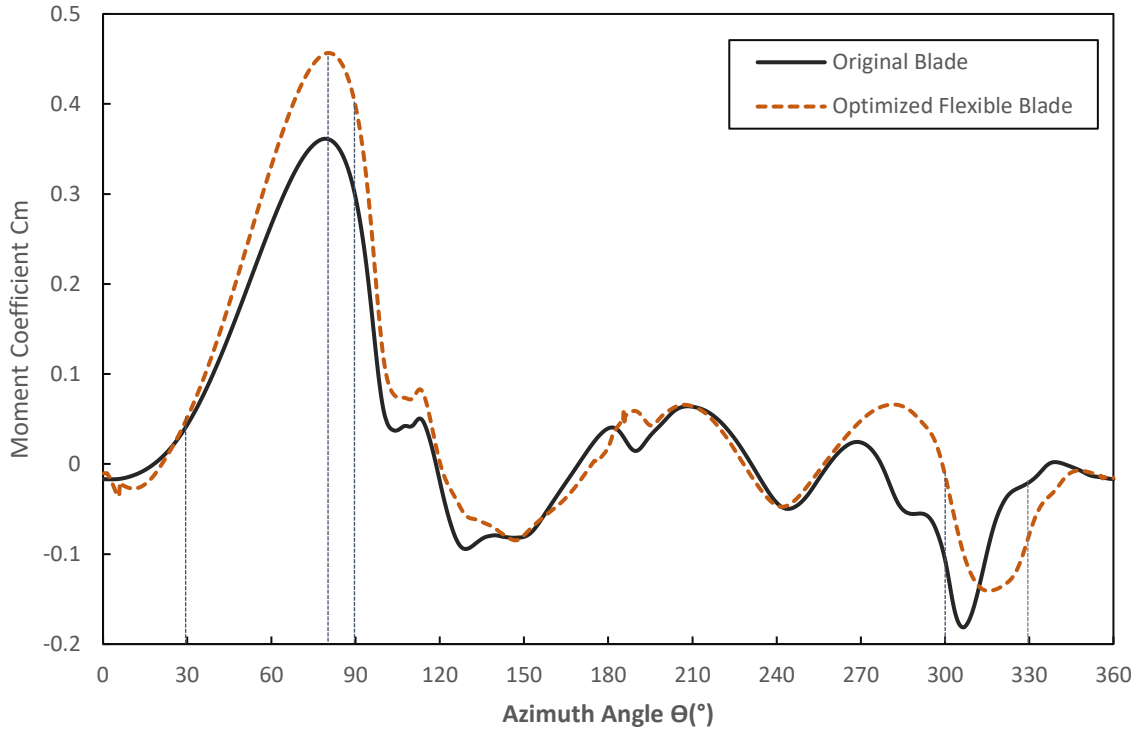
Figure 20: 2D Instantaneous moment coefficient of one blade for the two models at TSR=1.38

6.3.2 2D Static Pressure Contours

Figure 21 shows a comparison between pressure contours of the baseline turbine model and flexible blade turbine model at the locations specified in Figure 20 at $TSR = 1.38$. As shown at angles $\theta = 30°$, $\theta = 80°$, and $\theta = 90°$, a higher pressure was noticed at the pressure side of the deformed blades when compared to the original blade, creating a higher pressure difference between pressure and suction sides of the blade which consequently lead to higher power generated by the lift-driven turbine. In addition to that, at $\theta = 300°$, there is a higher pressure region near the trailing edge of the flexible blade model when compared to the baseline model which led to higher moment coefficient at this azimuthal position. On the other hand, at $\theta = 330°$, a lower pressure is noticed on both sides of the flexible model blade resulting in a lower aerodynamic performance when compared to the baseline model as shown in Figure 21.
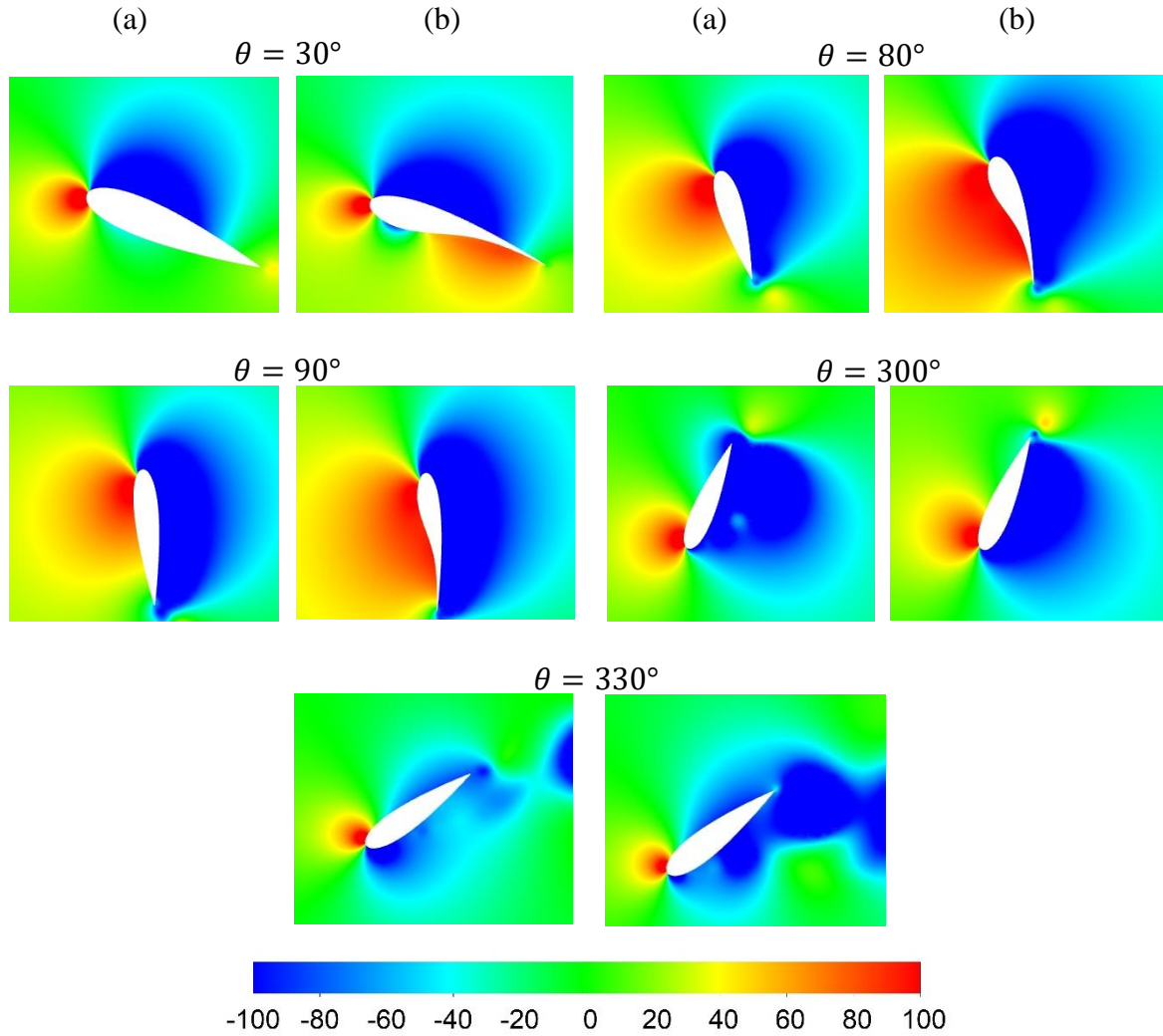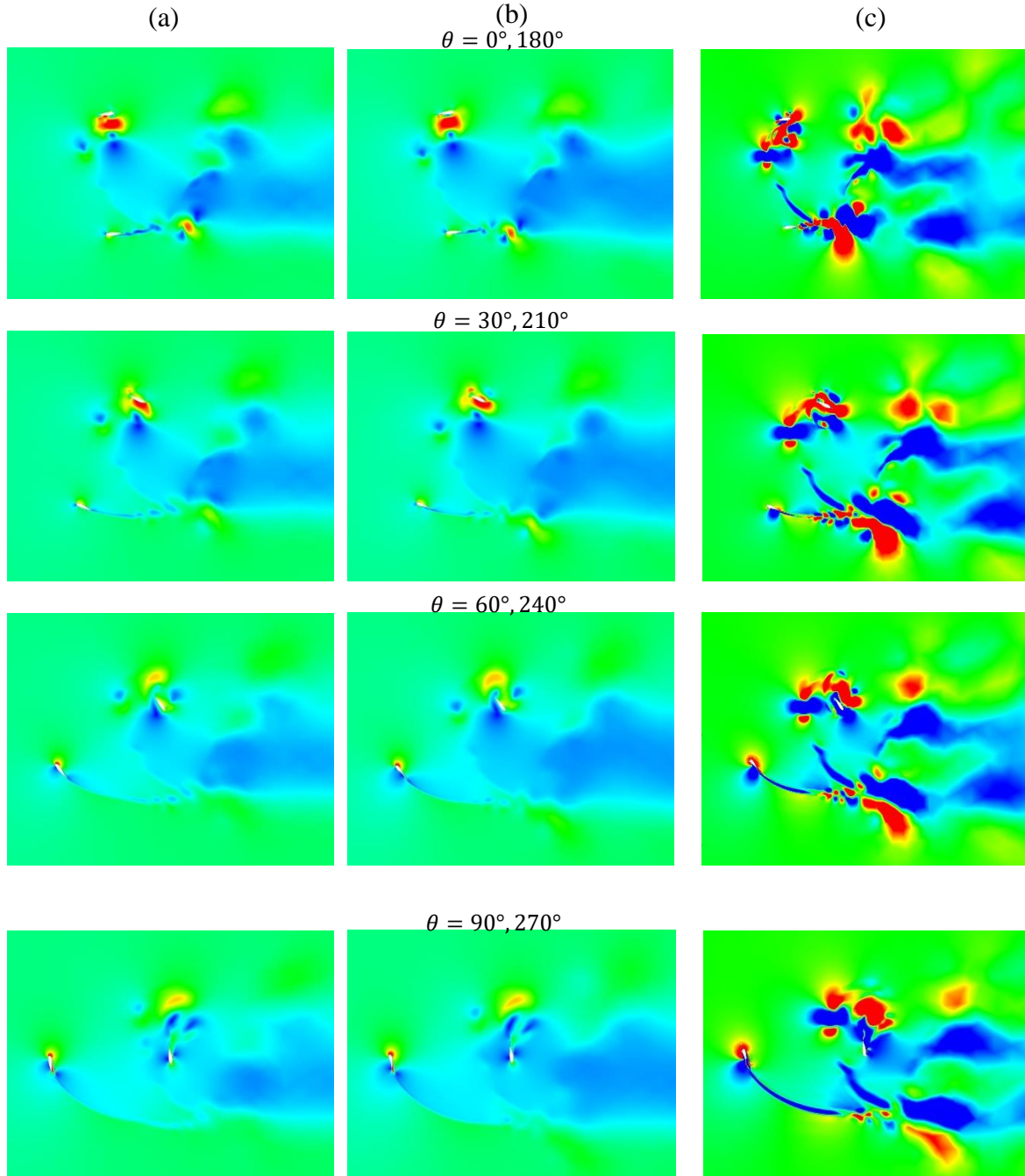
Figure 21: Comparison of pressure contours between baseline model (a) and flexible blade model (b) at TSR=1.38 at $\theta = 30°, 80°, 90°, 300°, and\ 330°$

6.3.3 2D Velocity Contours

Figure 22 shows the velocity contours at *TSR*=1.38 for the baseline model shown on the left side (a), the flexible turbine model in the middle (b) and the difference between velocity magnitude of both models on the right side (c). At $\theta = 30°, 60°$ and $90°$, a low velocity region is noticed at the pressure side of the blade near the trailing edge of the flexible blade whereas the baseline blade shows a higher velocity region in comparison. At $\theta = 120°$, a very high velocity region is present at the inner side of both the baseline and flexible blades, showing that the blades are experiencing a total dynamic stall which is also shown in the moment coefficient figure where a negative *Cm* values are obtained by the two models. At $\theta = 150°$ and $\theta = 180°$, the high velocity region separates from the surface of the blade, and at $\theta = 210°$, the blade interact with the high velocity region created at the

45

upwind side resulting in another decrease in the moment coefficient values as shown in Figure 20. At $\theta = 300°$, a more attached flow is noticed for the flexible turbine model blade leading to a higher instantaneous moment coefficient at this azimuthal position. It is also noticeable from the difference in velocity contours of both models shown in Figure 22 (c) that the flexible blade model shows a lower velocity values in the wake generated when compared to the baseline model showing that more energy is extracted from the upstream wind and led to a more depleted wake behind.
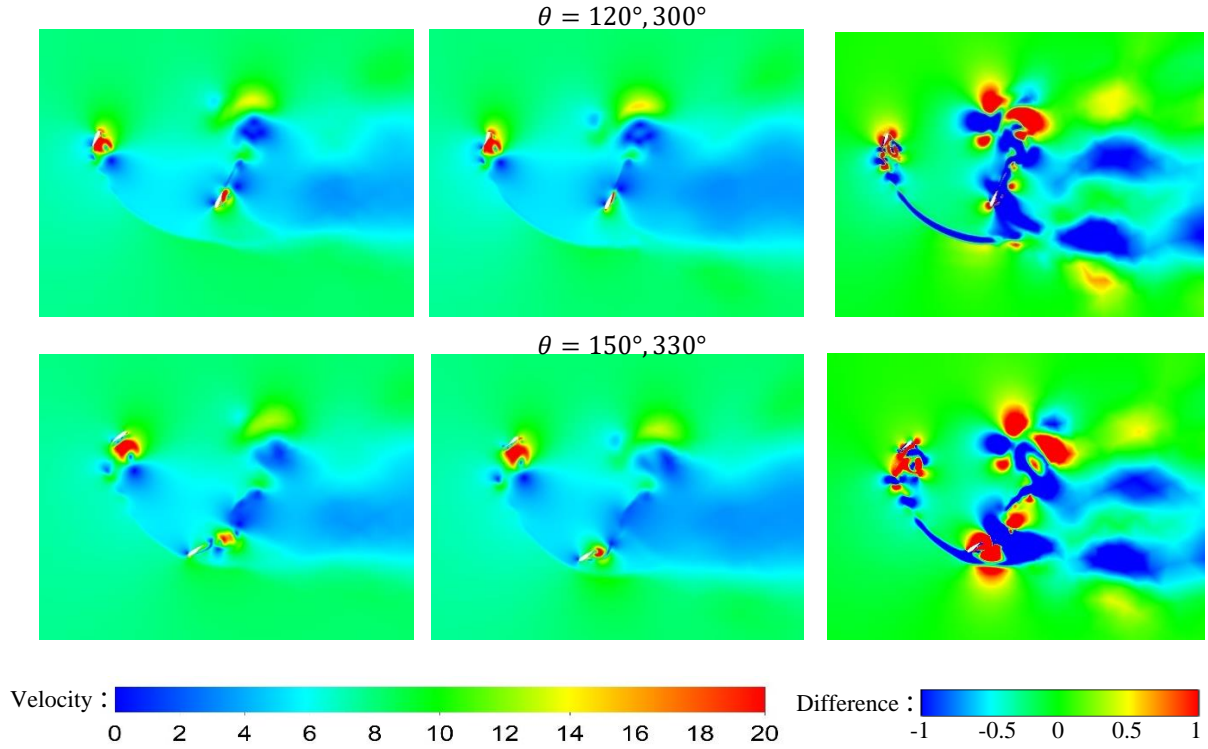
(a) (b) (c)

$\theta = 0°, 180°$

$\theta = 30°, 210°$

$\theta = 60°, 240°$

$\theta = 90°, 270°$

$$\theta = 120°, 300°$$

$$\theta = 150°, 330°$$

Velocity : 0 2 4 6 8 10 12 14 16 18 20

Difference : -1 -0.5 0 0.5 1

Figure 22: 2D Velocity contours for (a) Baseline model, (b) Flexible blade model, and (c) Difference between the two models at TSR=1.38

6.3.4 3D Instantaneous Moment Coefficient of One Blade

Instantaneous moment coefficients of both the baseline model and flexible blade model of the 3D CFD simulations at *TSR*=1.38 are calculated and presented in Figure 23. The deformed blade improved the output power of the turbine during the upwind side where the instantaneous moment coefficient reached a peak of 0.31 in comparison with the baseline model reaching 0.25, with a slightly lower performance around the azimuthal position $\theta = 180°$ where the blade switches from the deformed shape to the original shape. Then the moment coefficient of the new model follows the original one until $\theta = 300°$ where a higher aerodynamic performance is noticed for the flexible blade model.
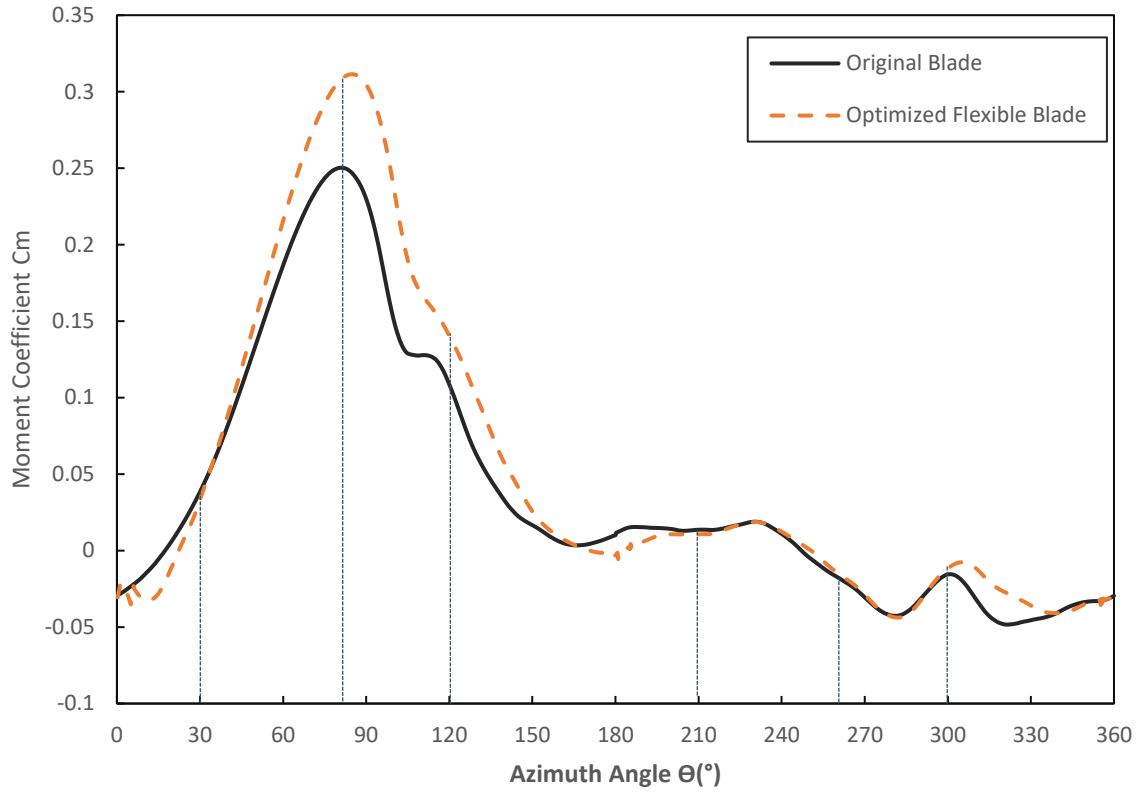
Figure 23: 3D Instantaneous moment coefficient of one blade for the two models at TSR=1.38

6.3.5 3D Q Criterion Contours

Figure 24 shows the iso-surfaces of Q-criterion=1000 coloured by velocity contours for the baseline turbine model and flexible blade turbine model at the locations specified in Figure 23 at *TSR*=1.38. Isometric views are used to illustrate the iso-surfaces at different blades positions throughout the full revolution of the turbine. At $\theta = 30°$, shedding appeared at the trailing edge of the flexible blade indicating flow detachment which resulted in a slightly lower performance than the baseline model. At $\theta = 80°$ and $\theta = 120°$, a thinner boundary layer and less shedding is noticed for the deformed blade indicating less flow separation and resulting in an improved flow around the blades which yielded a high moment coefficient. From $\theta = 180°$ to $210°$, the blade interacts with the tip vortex shedding created by the blade in the upwind side which caused a lower performance than the baseline model due to the stronger vortex created by the deformed blade in the upwind side. At $\theta = 260°$, Similar shedding is noticed in both baseline and flexible models which resulted in similar aerodynamic performance at this azimuthal position. At $\theta = 300°$, the flexible turbine model's blade has a slightly thinner boundary layer when compared to the baseline model which resulted in a slight increase in the moment coefficient.
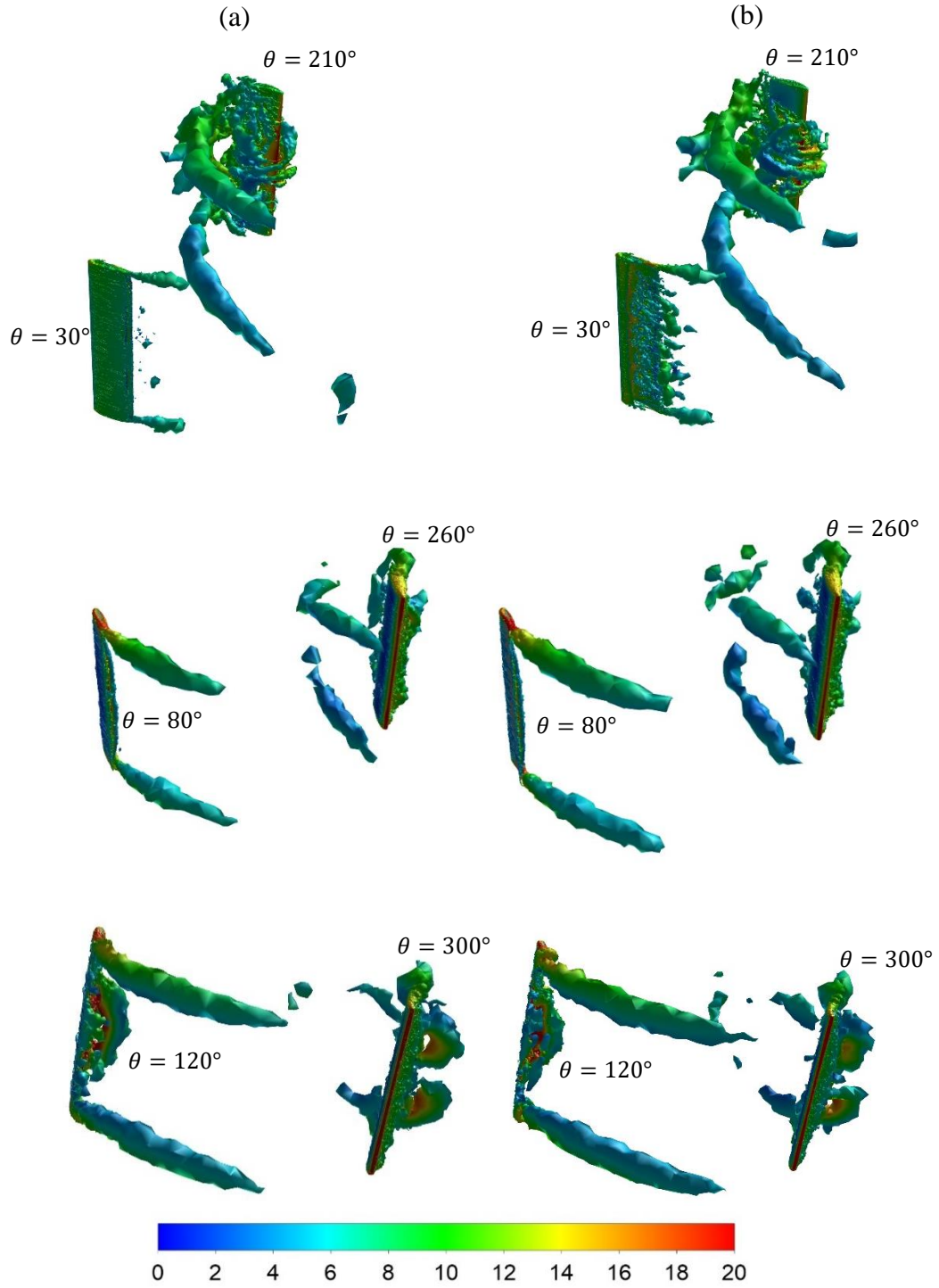
Figure 24: Iso-surfaces of Q=1000 coloured by velocity contours for (a) Baseline model and (b) Flexible blade model at TSR= 1.38

6.3.6 Flexible Blade Performance at high TSR values

To analysis the poor performance of the flexible blade model at high TSR values, iso-surfaces of vorticity magnitude =35 are plotted for the baseline and flexible turbine models at TSR=2.58. The parameters of the flexible blade used are $X_d/c = 0.9$, and $Y_d/Y_t = 0.5$ which yielded a power coefficient of 0.227 in comparison to the baseline model yielding 0.283. It was noticed that stronger shedding from the trailing edge and stronger tip blade vortex shedding from the deformed blade are causing the low aerodynamic performance of the new model. In addition to that, at high tip speed values, blades' interactions with the generated wake for the upwind side tend to become more dominant resulting in a lot of interactions that are causing a huge drop in the power coefficient as shown in Figure 25.
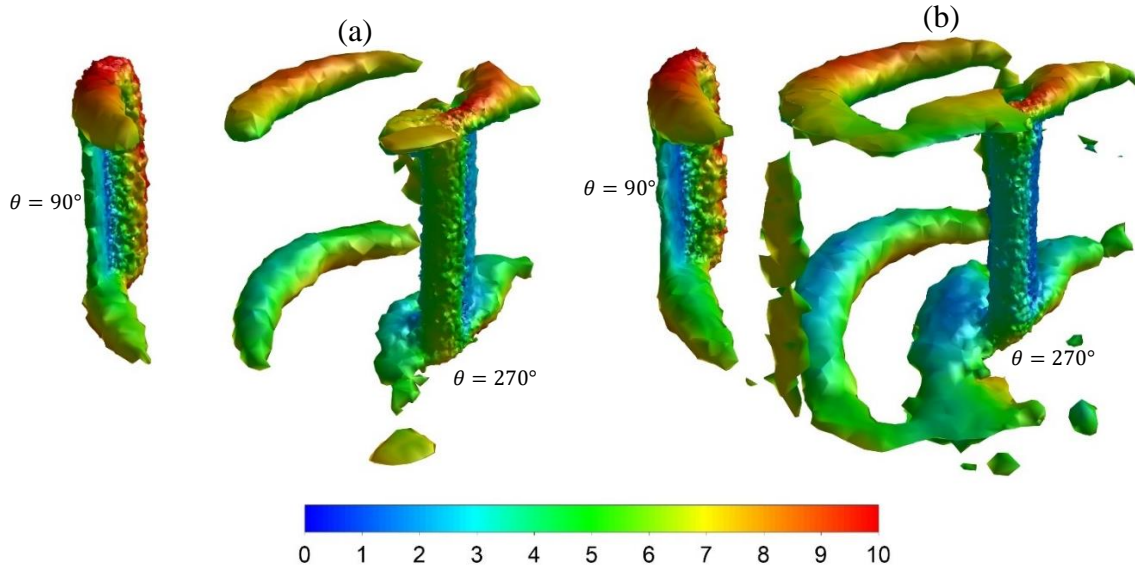

Figure 25: Iso-surfaces of Vorticity=35 coloured by velocity magnitude for (a) Baseline model and (b) Flexible blade model at TSR=2.58

CHAPTER SEVEN

CONCLUSIONS

The purpose of this study was to investigate the use of flexible blades for vertical axis wind turbine using numerical CFD simulations to enhance the aerodynamic performance of the turbine. To control the blades' nodes deformation, user defined functions alongside dynamic mesh were utilized in Ansys Fluent to conduct the simulations, and design of experiments method was applied to optimize the design parameters $(X_d/c, Y_d/Y_t)$ of the flexible blade at different tip speed ratios. In addition to that, optimization based on 2D and 3D CFD results were done to assess the use of 2D simulations for optimization purposes. Then, a detailed study of the power coefficient and the flow fields for the baseline model and the flexible blade model was performed and analyzed to explain the change in the turbine performance when rigid blades are replaced with flexible ones. The main findings of this study are as follows:

- Both 2D and 3D simulations showed a similar pattern in power coefficient improvement using the flexible blades where significant improvement was obtained at low *TSR* and gradually decreases as *TSR* increases.
- Optimized turbine model showed a 66% improvement over the baseline model for 2D simulations and 32% improvement for the 3D simulations.
- DOE results for both 2D and 3D simulations showed that *TSR* and interaction between Deformation Y_d/Y_t and *TSR* are the most influential factors.
- Highest performance improvement from both 2D and 3D simulations was obtained at TSR=1.38 with design parameters of $X_d/c = 0.9$, and $Y_d/Y_t = 0.5$.
- Optimization based on 2D and 3D results yielded the same optimum design parameters at low tip speed ratios ($X_d/c = 0.9$, $Y_d/Y_t = 0.5$) whereas at moderate tip speed ratios, both 2D and 3D results showed that $X_d/c = 0.9$ is the optimum while 2D results showed that $Y_d/Y_t = 0.5$ is optimum which is slightly different from 3D results with $Y_d/Y_t = 0.3$-0.4 as the optimum.
- Flow field analysis showed that blades interactions with the wake generated from upwind side increase as tip speed ratio increases resulting in poor performance for the flexible blade turbine model at high tip speed ratios.

For future studies, testing the proposed turbine model with wind tunnel experiments can validate the obtained results from CFD simulations and show the effectiveness using flexible blades for VAWT. In addition to that, an optimization study for the flexible blade design parameters at the downwind side can be carried out to further improve the turbine performance taking into account the practicality and complexity of the design when deforming the flexible blade at several azimuthal angles.

REFERENCES

[1]   Wang Y, Tong H, Sima H, Wang J, Sun J, Huang D. Experimental study on aerodynamic performance of deformable blade for vertical axis wind turbine. Energy 2019;181:187–201. https://doi.org/10.1016/J.ENERGY.2019.03.181.

[2]   Sun J, Sun X, Huang D. Aerodynamics of vertical-axis wind turbine with boundary layer suction – Effects of suction momentum. Energy 2020;209:118446. https://doi.org/10.1016/j.energy.2020.118446.

[3]   Wong KH, Chong WT, Sukiman NL, Poh SC, Shiah YC, Wang CT. Performance enhancements on vertical axis wind turbines using flow augmentation systems: A review. Renew Sustain Energy Rev 2017;73:904–21. https://doi.org/10.1016/j.rser.2017.01.160.

[4]   Wang Z, Zhuang M. Leading-edge serrations for performance improvement on a vertical-axis wind turbine at low tip-speed-ratios. Appl Energy 2017;208:1184–97. https://doi.org/10.1016/J.APENERGY.2017.09.034.

[5]   Yousefi Roshan M, Khaleghinia J, Eshagh Nimvari M, Salarian H. Performance improvement of Darrieus wind turbine using different cavity layouts. Energy Convers Manag 2021;246:114693. https://doi.org/10.1016/J.ENCONMAN.2021.114693.

[6]   Liu J, Lin H, Zhang J. Review on the technical perspectives and commercial viability of vertical axis wind turbines. Ocean Eng 2019;182:608–26. https://doi.org/10.1016/J.OCEANENG.2019.04.086.

[7]   Ghasemian M, Ashrafi ZN, Sedaghat A. A review on computational fluid dynamic simulation techniques for Darrieus vertical axis wind turbines. Energy Convers Manag 2017;149:87–100. https://doi.org/10.1016/J.ENCONMAN.2017.07.016.

[8]   Li Q, Maeda T, Kamada Y, Murata J, Kawabata T, Shimizu K, et al. Wind tunnel and numerical study of a straight-bladed vertical axis wind turbine in three-dimensional analysis (Part I: For predicting aerodynamic loads and performance). Energy 2016;106:443–52. https://doi.org/10.1016/J.ENERGY.2016.03.089.

[9]   Rezaeiha A, Montazeri H, Blocken B. Characterization of aerodynamic performance of vertical axis wind turbines: Impact of operational parameters. Energy Convers Manag 2018;169:45–77. https://doi.org/10.1016/J.ENCONMAN.2018.05.042.

[10] Hand B, Kelly G, Cashman A. Aerodynamic design and performance parameters of a lift-type vertical axis wind turbine: A comprehensive review. Renew Sustain Energy Rev 2021;139:110699. https://doi.org/10.1016/J.RSER.2020.110699.

[11] Rezaeiha A, Montazeri H, Blocken B. On the accuracy of turbulence models for CFD simulations of vertical axis wind turbines. Energy 2019;180:838–57. https://doi.org/10.1016/J.ENERGY.2019.05.053.

[12] Xu W, Li G, Zheng X, Li Y, Li S, Zhang C, et al. High-resolution numerical simulation of the performance of vertical axis wind turbines in urban area: Part I, wind turbines on the side of single building. Renew Energy 2021;177:461–74. https://doi.org/10.1016/J.RENENE.2021.04.071.

[13] Rezaeiha A, Montazeri H, Blocken B. Towards optimal aerodynamic design of vertical axis wind turbines: Impact of solidity and number of blades. Energy 2018;165:1129–48. https://doi.org/10.1016/J.ENERGY.2018.09.192.

[14] Hao W, Bashir M, Li C, Sun C. Flow control for high-solidity vertical axis wind turbine based on adaptive flap. Energy Convers Manag 2021;249:114845. https://doi.org/10.1016/J.ENCONMAN.2021.114845.

[15] Zhu H, Hao W, Li C, Ding Q, Wu B. A critical study on passive flow control techniques for straight-bladed vertical axis wind turbine. Energy 2018;165:12–25. https://doi.org/10.1016/J.ENERGY.2018.09.072.

[16] Acarer S. Peak lift-to-drag ratio enhancement of the DU12W262 airfoil by passive flow control and its impact on horizontal and vertical axis wind turbines. Energy 2020;201:117659. https://doi.org/10.1016/J.ENERGY.2020.117659.

[17] Ferreira CS, Geurts B, Ferreira CS, Geurts B. Aerofoil optimization for vertical-axis wind turbines. Wind ENERGY Wind Energ 2015;18:1371–85. https://doi.org/10.1002/we.1762.

[18] De Tavernier D, Ferreira C, van Bussel G. Airfoil optimisation for vertical-axis wind turbines with variable pitch. Wind Energy 2019;22:547–62. https://doi.org/10.1002/WE.2306.

[19] Bouzaher MT, Hadid M, Semch-Eddine D. Flow control for the vertical axis wind turbine by means of flapping flexible foils. J Brazilian Soc Mech Sci Eng 2017;39:457–70. https://doi.org/10.1007/S40430-016-0618-3/FIGURES/19.

[20] Leonczuk Minetto RA, Paraschivoiu M. Simulation based analysis of morphing blades applied to a vertical axis wind turbine. Energy 2020;202:117705.

https://doi.org/10.1016/J.ENERGY.2020.117705.

[21]   MacPhee DW, Beyene A. Fluid–structure interaction analysis of a morphing vertical axis wind turbine. J Fluids Struct 2016;60:143–59. https://doi.org/10.1016/J.JFLUIDSTRUCTS.2015.10.010.

[22]   Baghdadi M, Elkoush S, Akle B, Elkhoury M. Dynamic shape optimization of a vertical-axis wind turbine via blade morphing technique. Renew Energy 2020;154:239–51. https://doi.org/10.1016/J.RENENE.2020.03.015.

[23]   Wang Y, Sun X, Dong X, Zhu B, Huang D, Zheng Z. Numerical investigation on aerodynamic performance of a novel vertical axis wind turbine with adaptive blades. Energy Convers Manag 2016;108:275–86. https://doi.org/10.1016/J.ENCONMAN.2015.11.003.

[24]   Zeiner-Gundersen DH. A novel flexible foil vertical axis turbine for river, ocean, and tidal applications. Appl Energy 2015;151:60–6. https://doi.org/10.1016/J.APENERGY.2015.04.005.

[25]   Hoerner S, Abbaszadeh S, Maître T, Cleynen O, Thévenin D. Characteristics of the fluid–structure interaction within Darrieus water turbines with highly flexible blades. J Fluids Struct 2019;88:13–30. https://doi.org/10.1016/J.JFLUIDSTRUCTS.2019.04.011.

[26]   Li Q, Maeda T, Kamada Y, Murata J, Furukawa K, Yamamoto M. The influence of flow field and aerodynamic forces on a straight-bladed vertical axis wind turbine. Energy 2016;111:260–71. https://doi.org/10.1016/j.energy.2016.05.129.

[27]   Rezaeiha A, Kalkman I, Blocken B. CFD simulation of a vertical axis wind turbine operating at a moderate tip speed ratio: Guidelines for minimum domain size and azimuthal increment. Renew Energy 2017;107:373–85. https://doi.org/10.1016/j.renene.2017.02.006.

[28]   Balduzzi F, Bianchini A, Maleci R, Ferrara G, Ferrari L. Critical issues in the CFD simulation of Darrieus wind turbines. Renew Energy 2016;85:419–35. https://doi.org/10.1016/J.RENENE.2015.06.048.

[29]   Li Q, Maeda T, Kamada Y, Murata J, Furukawa K, Yamamoto M. Effect of number of blades on aerodynamic forces on a straight-bladed Vertical Axis Wind Turbine. Energy 2015;90:784–95. https://doi.org/10.1016/J.ENERGY.2015.07.115.

[30]   Zhang T tian, Elsakka M, Huang W, Wang Z guo, Ingham DB, Ma L, et al. Winglet design for vertical axis wind turbines based on a design of experiment and CFD

approach. Energy Convers Manag 2019;195:712–26. https://doi.org/10.1016/J.ENCONMAN.2019.05.055.

[31]   Wang Z, Wang Y, Zhuang M. Improvement of the aerodynamic performance of vertical axis wind turbines with leading-edge serrations and helical blades using CFD and Taguchi method. Energy Convers Manag 2018;177:107–21. https://doi.org/10.1016/J.ENCONMAN.2018.09.028.

[32]   Attie C, ElCheikh A, Nader J, Elkhoury M. Performance enhancement of a vertical axis wind turbine using a slotted deflective flap at the trailing edge. Energy Convers Manag 2022;273:116388. https://doi.org/10.1016/J.ENCONMAN.2022.116388.

APPENDIX

UDF CODE

```
#include "udf.h"
#include "math.h"
#include "unsteady.h"
#include "dynamesh_tools.h"
DEFINE_GRID_MOTION(Inward2blades, domain, dt, time, dtime)
{
Thread *tf = DT_THREAD(dt);
face_t f;
Node *v;
int n,ii;
double a0[40] = {};
double a1[40] ={} ;
double b1[40] = {};
double a2[40] = {};
double b2[40] ={};
double a3[40] = {};
double b3[40] ={};
double a4[40] ={};
double b4[40] ={};
double a5[40] = {};
double b5[40] ={};
double a6[40] = {};
double b6[40] ={};
double w[40] = {};
double x;
double e=CURRENT_TIME;
double omegaw=17.52;
double theta=CURRENT_TIME*omegaw;
double theta_degree =theta*360/(2*M_PI);
double value =0;
if (theta_degree>360)
{
if(fmod(theta_degree, 360)!=0)
{
value =theta_degree-360*(int)(theta_degree/360);
}
else
{
value =360;
}
}
else
{
value =theta_degree;
```

```
}
int cur=N_TIME%1440;
SET_DEFORMING_THREAD_FLAG(THREAD_T0(tf));
begin_f_loop(f, tf)
{
f_node_loop(f, tf, n)
{
v = F_NODE(f, tf, n);
if (NODE_POS_NEED_UPDATE(v))
{
if(NODE_Y(v)<0)
{
if(value<4.85 || value>359.8)
{
x=NODE_X(v);
NODE_Y(v)= a0[cur] +a1[cur]*cos(x*w[cur]) +b1[cur]*sin(x*w[cur])
+a2[cur]*cos(2*x*w[cur]) + b2[cur]*sin(2*x*w[cur]) +a3[cur]*cos(3*x*w[cur]) +
b3[cur]*sin(3*x*w[cur]) +  a4[cur]*cos(4*x*w[cur]) +  b4[cur]*sin(4*x*w[cur]) +
a5[cur]*cos(5*x*w[cur]) + b5[cur]*sin(5*x*w[cur]) + a6[cur]*cos(6*x*w[cur]) +
b6[cur]*sin(6*x*w[cur]);
NODE_POS_UPDATED(v);
}
if(value>179.85 && value<184.85)
{
x=NODE_X(v);
NODE_Y(v)= a0[cur-720] +a1[cur-720]*cos(x*w[cur-720]) +b1[cur-720]*sin(x*w[cur-
720]) +a2[cur-720]*cos(2*x*w[cur-720]) + b2[cur-720]*sin(2*x*w[cur-720]) +a3[cur-
720]*cos(3*x*w[cur-720]) + b3[cur-720]*sin(3*x*w[cur-720]) +  a4[cur-
720]*cos(4*x*w[cur-720]) +  b4[cur-720]*sin(4*x*w[cur-720]) +  a5[cur-
720]*cos(5*x*w[cur-720]) + b5[cur-720]*sin(5*x*w[cur-720]) + a6[cur-
720]*cos(6*x*w[cur-720]) + b6[cur-720]*sin(6*x*w[cur-720]);
NODE_POS_UPDATED(v);
}
}
if(NODE_Y(v)>0)
{
if(value>354.9 && value<359.8)
{
x=NODE_X(v);
NODE_Y(v)= a0[cur-1420+20] +a1[cur-1420+20]*cos(x*w[cur-1420+20]) +b1[cur-
1420+20]*sin(x*w[cur-1420+20]) +a2[cur-1420+20]*cos(2*x*w[cur-1420+20]) +
b2[cur-1420+20]*sin(2*x*w[cur-1420+20]) +a3[cur-1420+20]*cos(3*x*w[cur-1420+20])
+ b3[cur-1420+20]*sin(3*x*w[cur-1420+20]) +  a4[cur-1420+20]*cos(4*x*w[cur-
1420+20]) +  b4[cur-1420+20]*sin(4*x*w[cur-1420+20]) +  a5[cur-
1420+20]*cos(5*x*w[cur-1420+20]) + b5[cur-1420+20]*sin(5*x*w[cur-1420+20]) +
a6[cur-1420+20]*cos(6*x*w[cur-1420+20]) + b6[cur-1420+20]*sin(6*x*w[cur-
1420+20]);
NODE_POS_UPDATED(v);
}
```

```
if(value>174.9 && value<179.85)
{
x=NODE_X(v);
NODE_Y(v)= a0[cur-700+20] +a1[cur-700+20]*cos(x*w[cur-700+20]) +b1[cur-
700+20]*sin(x*w[cur-700+20]) +a2[cur-700+20]*cos(2*x*w[cur-700+20]) + b2[cur-
700+20]*sin(2*x*w[cur-700+20]) +a3[cur-700+20]*cos(3*x*w[cur-700+20]) + b3[cur-
700+20]*sin(3*x*w[cur-700+20]) +  a4[cur-700+20]*cos(4*x*w[cur-700+20]) + b4[cur-
700+20]*sin(4*x*w[cur-700+20]) +  a5[cur-700+20]*cos(5*x*w[cur-700+20]) + b5[cur-
700+20]*sin(5*x*w[cur-700+20]) + a6[cur-700+20]*cos(6*x*w[cur-700+20]) + b6[cur-
700+20]*sin(6*x*w[cur-700+20]);
NODE_POS_UPDATED(v);
}
}
}
}
}
end_f_loop(f, tf);
}
```